J. Fluid Mech. (1989), *vol.* 201, *pp.* 379–410
Printed in Great Britain

Transition to chaos in a differentially heated vertical cavity

By SAMUEL PAOLUCCI AND DONALD R. CHENOWETH
Applied Mechanics Department, Sandia National Laboratories, Livermore, CA 94550, USA

(Received 10 December 1987)

We investigate numerically the transition from laminar to chaotic flow of a Boussinesq fluid with $Pr = 0.71$ in two-dimensional closed, differentially heated, vertical cavities having aspect ratios near unity. The cavities have rigid conducting sidewalls, and rigid insulating top and bottom walls. The physical nature of the resulting flow is a function of the aspect ratio and Rayleigh number.

It is shown that an oscillatory approach to steady-state, oscillatory instabilities, quasi-periodic flow, and chaotic flow exist for the flow regimes investigated. We find that for aspect ratios of approximately three or larger the the first transition from steady-state is due to instability of the sidewall boundary layers, while for smaller aspect ratios, but larger than $\frac{1}{2}$, it is due to internal waves near the departing corners. For both instabilities we obtain the critical Rayleigh number as a function of aspect ratio and write expressions relating the fundamental frequencies of the oscillatory flow to the Rayleigh number and aspect ratio. When Ra is increased significantly above the first critical value, the flow becomes complex since both types of instabilities can be present. With a further increase in Rayleigh number the flow becomes chaotic and eventually turbulent. The above results are illustrated for different Rayleigh numbers and aspect ratios using time histories, spectral analysis, and streamlines at different values of time.

1. Introduction

Thermal convection in differentially heated cavities has been studied extensively because of its relevance in a number of diverse fields. The majority of prior work in this area has been concerned with steady-state laminar flow. Yet in many of the fields of application, the flow is unsteady and possibly turbulent. Since many variables of engineering interest depend strongly on the flow regime, it is essential to understand the different physical processes responsible for the conversion of an initially laminar flow to a turbulent one. The present study addresses the oscillatory approach to steady-state and the transition from steady-state to turbulence via two-dimensional direct numerical simulations. The problem becomes stiff owing to a decrease in boundary-layer thickness with increasing Rayleigh number Ra. As a result, there has been very little numerical work performed in this area.

Gill & Davey (1969) and Bergholtz (1978) performed two-dimensional linear stability analyses of the buoyancy layers that form on the vertical walls. They showed that at a certain Rayleigh number the boundary layers become oscillatory. The stability of our problem is very closely related to that of the buoyancy layer since for large Ra the stratification in the cavity is approximately constant in the horizontal direction and linear in the vertical direction, except near the walls. However, we show (see §3.1.2) that their results applied to finite cavities (using a

thermal stratification parameter near unity) yield a critical wavelength of the vertical wall boundary layer $\lambda_c \sim A/Pr^n$, where A is the aspect ratio, and $n \leqslant \frac{1}{2}$; thus the applicability of their results to finite cavities is questionable for small Prandtl numbers since we find $\lambda_c \approx 0.3A$ for $Pr = 0.71$, where $n \approx 0$. Iyer (1973) showed that two-dimensional transverse waves are the most unstable in the buoyancy layer, thus indicating that our two-dimensional assumption is not unreasonable. However, it is not clear that this assumption will remain valid in the nonlinear regime. Furthermore, we note that their analyses cannot yield any possible instabilities due to the presence of the horizontal walls.

By including endwall effects, Patterson & Imberger (1980) suggested a relatively simple criterion for the presence of internal wave oscillations when $Pr \geqslant 1$ and $A \leqslant 1$. Furthermore, they concluded that cavity-scale internal wave activity is due to a 'pile up' of the horizontal intrusions at the far ends. Ivey (1984) performed experiments in a square cavity at Rayleigh numbers of the order of 10^9 using water as the working fluid. He emphasized the importance of the inertia effect of the flow and his results show that damped oscillations arise from internal hydraulic jumps caused by the turning of the vertical boundary layers. Since the source is localized, he further concludes that due to rapid attenuation, their presence could not be felt throughout the cavity as Patterson & Imberger suggest. The numerical results of Chenoweth & Paolucci (1986) seem to be in agreement with Ivey's conclusions; furthermore, they also suggest that for low aspect ratios the 'hydraulic' jumps are responsible for the first transition to time-dependent flow.

Le Quere & Alziary de Roquefort (1985*a*) used a semi-implicit Chebyshev spectral method to examine the oscillatory approach to steady state of the average Nusselt number for $A = 1$, $Pr = 0.71$, and $Ra = 10^7$ and 4×10^7. For $Ra = 4 \times 10^7$ they note the presence of detached regions near the departing corners at steady state. These regions were also present at $Ra = 10^7$, but in this case they did not persist to steady state. Subsequently, Le Quere & Alziary de Roquefort (1986) computed the first transition to periodic flow for A as low as 2 and concluded that in all cases the time-dependent periodic motion is a result of wall-boundary-layer instability. However, for $A < 3$ they did note the presence of separated flow regions along the horizontal walls which remained when the flow was observed to be statistically stationary. Haldenwang (1986), also using a semi-implicit Chebyshev spectral method, computed the solution for $A = 1$, $Pr = 0.71$, and $Ra = 10^6$, $10^{6.5}$, 10^7, $10^{7.5}$, 10^8, and $10^{8.5}$. He concluded that: regions of reverse flow on the horizontal walls are present for $Ra \geqslant 10^{7.5}$; the flow becomes oscillatory for Ra between 10^8, and $10^{8.5}$ where two fundamental frequencies were observed; and that these two frequencies, neither of which is in continuity with the one observed at smaller Rayleigh numbers, are first observed in the stable solution at $Ra = 10^8$.

In this paper we clarify the basic mechanism of steady and unsteady oscillatory motion in a rectangular cavity with one heated and one cooled vertical wall and two adiabatic horizontal ends. Simulations are performed for a Boussinesq fluid with $Pr = 0.71, \frac{1}{2} \leqslant A \leqslant 3$, and a wide range of Rayleigh numbers. Our restriction to two spatial dimensions precludes possibly important three-dimensional nonlinear effects due to vortex stretching. But even within our limitations, imposed by present day computers, the simpler model is of interest in providing insight into the physical mechanisms which drive the convective dynamics from laminar to turbulent flows. Furthermore, while it is an accepted fact that the laminar flow is inherently two-dimensional (see Eckert & Carlson 1961), some experiments indicate that even the

resulting turbulent flow is dominated by two-dimensional structures (e.g. Elder 1965). The goal behind the numerical experiments is to study the transitions to various time-dependent flows. With increasing Rayleigh number the onset of periodic flow is calculated for various aspect ratios. Power spectra of the temperature and the velocity components are examined, and their dependence on the location probed is discussed. We are primarily concerned with instabilities that precede turbulence rather than strongly turbulent flows, although we also look at the oscillatory approach to steady-state for high Rayleigh numbers. Due to a lack of a closed form analytical solution, we study the loss of instability to time dependent flow by direct numerical simulation. This approach allows us to obtain solutions for large supercritical values of the Rayleigh number. All of our simulations satisfy a criterion for the presence of internal wave activity similar to that of Patterson & Imberger (1980), but for $Pr \leqslant 1$ and arbitrary A. In agreement with Patterson & Imberger we show that within this region of parameter space the flow approaches steady-state conditions in an oscillatory fashion, although the source of the oscillations is different to that suggested by them. In agreement with Ivey's (1984) experimental results we find that the oscillatory behaviour is due to the inertia of the flow entering the interior of the cavity from the sidewall boundary layers (departing corners), which leads to a form of internal 'hydraulic' jump when the Rayleigh number is sufficiently large. The onset and frequencies of the oscillatory instabilities are calculated and compared with available data. We present numerical experiments which exhibit repeated supercritical branching leading to chaotic flow after a finite number of bifurcations. A sequence of instabilities quite similar to that described in this paper has been observed by Gollub & Benson (1980) in a laser-Doppler velocimetry study of Rayleigh–Bénard convection and also by Fenstermacher, Swinney & Gollub (1979) and Gorman & Swinney (1982) in the Couette–Taylor system. In particular, the velocity spectra show a periodic regime with a single fundamental frequency followed by a quasi-periodic regime with two fundamental frequencies, and then broadband noise components appear in the spectra. Finally, the amplitude of the sharp frequency components decrease with increasing Rayleigh number.

2. Analysis

2.1. *Problem description*

Consider a two-dimensional rectangular enclosure of width L and height H filled with a gas. The left and right walls of the cavity are maintained at temperatures of T_h and T_c, respectively, where $T_h > T_c$. The top and bottom walls are insulated. We non-dimensionalize the problem by reference quantities for length, velocity and temperature using the cavity width L, the thermal diffusion speed α/L, and the mean of the wall temperatures $T_r = \frac{1}{2}(T_h + T_c)$, respectively.

The problem evolves in time t and can be described in terms of the velocity components $v_i = (u, v)$ in the $x_i = (x, y)$-directions, temperature T, and pressure p. The governing equations are statements of conservation of mass, momentum, and energy. The equations, valid under a small Mach number approximation, have been previously used by Chenoweth & Paolucci (1986) and are given as follows:

$$\frac{\partial \rho}{\partial t} + \frac{\partial \rho v_j}{\partial x_j} = 0, \tag{2.1}$$

$$\frac{\partial \rho v_i}{\partial t}+\frac{\partial}{\partial x_j}(\rho v_j v_i) = -\frac{\partial \Pi}{\partial x_i}+\frac{Ra\,Pr}{2\epsilon}\rho n_i + Pr\frac{\partial}{\partial x_j}\tau_{ij}, \tag{2.2}$$

$$\rho c_p\left(\frac{\partial T}{\partial t}+v_j\frac{\partial T}{\partial x_j}\right)-\Gamma\frac{d\bar{p}}{dt} = \frac{\partial}{\partial x_j}\left(k\frac{\partial T}{\partial x_j}\right), \tag{2.3}$$

$$\rho = \rho(\bar{p}, T), \tag{2.4}$$

where $\Pi = p^{(1)}/(\gamma Ma^2)$ is a reduced pressure which accounts for the hydrostatic and dynamic effects, $p^{(1)}$ is the second term in the Mach number expansion of p and is $O(Ma^2)$, γ is the ratio of specific heats, n_i is the unit vector in the direction of gravity, τ_{ij} is the viscous stress tensor given by

$$\tau_{ij} = \mu\left(\frac{\partial v_i}{\partial x_j}+\frac{\partial v_j}{\partial x_i}\right)-\tfrac{2}{3}\delta_{ij}\mu\frac{\partial v_k}{\partial x_k},$$

δ_{ij} is the Kronecker delta function, and $\Gamma = (\gamma-1)/\gamma$ is a measure of the resilience of the fluid. The thermal conductivity, viscosity, and specific heat at constant pressure are functions of the thermodynamic variables. Note that the Mach number only serves as a scaling for the dynamic and hydrostatic components of pressure.

The spatially uniform pressure $\bar{p} = p^{(0)}(t)$ appearing in the energy equation and the equation of state, which represents the first term in the expansion of p, accounts for the change of the static pressure with time. The separation of the pressure components, holding under the small Mach number approximation, is the essence of the acoustic wave 'filtering'; however this splitting introduces $\bar{p}$ as an extra unknown. It can be shown that the equation for $\bar{p}$, is obtained by a global mass conservation statement and the use of boundary conditions.

The dimensionless boundary conditions are:

$$\left.\begin{aligned} v_i(0,y,t) = v_i(1,y,t) = v_i(x,0,t) = v_i(x,A,t) = 0,\\ T(0,y,t) = 1+\epsilon, \quad T(1,y,t) = 1-\epsilon,\\ \frac{\partial T}{\partial y}(x,0,t) = \frac{\partial T}{\partial y}(x,A,t) = 0. \end{aligned}\right\} \tag{2.5}$$

In the Boussinesq limit $\epsilon\to 0$ the relevant independent dimensionless parameters are

$$A = \frac{H}{L}, \quad Pr = \frac{\nu}{\alpha}, \quad Ra = \frac{\beta g \Delta T L^3}{\nu\alpha}, \tag{2.6}$$

where β is the coefficient of volume expansion and $\Delta T = T_h - T_c$. The parameters in (2.6) represent the aspect ratio, the Prandtl number, and the Rayleigh number, respectively. In this paper we treat only the case $Pr = 0.71$. Since (2.1)–(2.4) include non-Boussinesq effects, in all cases we use $\Delta T/T_r = 2\epsilon = 0.01$ to obtain results near the Boussinesq limit. We note that in this limit $\bar{p}\to 1$.

For each aspect ratio, steady-state solutions for the largest Rayleigh numbers in Chenoweth & Paolucci (1986) were used for initial conditions. Thereafter, with the exceptions noted, each computation for larger values of Ra was started from the stationary flow of the closest lower Rayleigh number. A flow whose statistical properties do not vary with time is said to be stationary. A weakly stationary flow of second order is one which has a constant mean and variance at any arbitrary location in the flow. Our solutions are weakly stationary to second order only within a certain accuracy (see §2.3) since the first two moments are only approximately

independent of time. We note that had the Boussinesq equations been used, because of the symmetric properties of the problem, the resulting laminar flows would have been *exactly* centro-symmetric even at the large Rayleigh numbers treated in the present paper. To move the solution from mathematically unstable branches an arbitrary artificial perturbation would have been required. In contrast the above anelastic equations, which treat property variations consistently, do not possess the symmetric properties for any finite value of ϵ, and hence physically unrealizable unstable solution branches cannot be obtained. Furthermore, we believe that the path through transition is more representative of the real physical problem since the properties of the gas properly specify the degree of asymmetry and the amplitude of the 'perturbation'. With this understanding, we caution the reader that when we say that a flow is 'symmetric', we actually mean that it is symmetric to within $O(\epsilon)$.

2.2. *Numerical procedure*

We solved the governing equations (2.1)–(2.4) using primitive variables on a staggered mesh with an explicit predictor–corrector finite-difference method using forward differences for time derivatives and central differences for spatial derivatives, with a truncation error $O(\Delta t, \Delta x^2)$.

There are several ways to formally deduce a finite difference scheme from the basic equations. To derive the finite difference equations we discretized the physical domain in the (x, y)-plane with three interlacing staggered meshes. One for the horizontal velocity component, one for the vertical velocity component, and one for all scalar variables. The position of the grid points and their spacings are chosen such that the fluid boundaries lie between scalar points. Thus, the top and bottom boundaries go through v points, and the vertical boundaries go through u points. One layer of grid points outside the region of interest is included to facilitate the application of boundary conditions. The governing equations are averaged on a local two-dimensional grid volume defined by $\Delta V_{i,j} = \Delta x_i \Delta y_j$ to obtain their finite difference form. This procedure is described by Grötzbach (1982), where the reader is referred for more details.

The fluid velocity is prescribed on the boundaries of the cavity. This is done in two different ways: at those points lying on a boundary we fix the corresponding velocity component to the desired value; for those components for which the computational points do not fall on a boundary, we force two interior points and the point exterior to the boundary to have the desired values by adjusting the velocity at the outside points by quadratic extrapolation. Temperature points do not lie on any boundary. Hence, we force two interior points and the point exterior to the boundary to yield the specified constant temperature on the vertical walls and a zero flux on the horizontal walls by quadratic extrapolations. The boundary conditions for the pressure are obtained by evaluating the momentum equations at the walls. Even though the computations are done using primitive variables, all velocity field results are presented in terms of the stream function (valid in the Boussinesq limit)

$$u = \frac{\partial \psi}{\partial y}, \quad v = -\frac{\partial \psi}{\partial x}, \tag{2.7}$$

to facilitate the display of the flow field.

In order to accurately describe gradients in the wall boundary layers at large Rayleigh numbers, it is necessary to use a non-uniform coordinate mesh. The need for non-uniform grids arises since in some cases the smallest grids necessary near the boundaries are much smaller than those needed well outside the boundary layers.

The approach used is a simple one. The grids are spaced non-uniformly in a manner to be described shortly. We transform the non-uniform Δx_i and Δy_j in the finite difference equations to a uniform grid using the orthogonal transformation $\xi_k = \xi_k(x_k)$ which also maps the problem to the computational domain $-1 \leqslant \xi_k \leqslant 1$, where $x_k = (x, y)$ and $\xi_k = (\xi, \eta)$. An accurate transformed central finite difference equation for the first difference operator is given by Kálnay de Rivas (1972)

$$\left(\frac{\partial f}{\partial y}\right)_j = \frac{f_{j+1} - f_{j-1}}{2\Delta\eta(\partial y/\partial\eta)_j(1+\frac{1}{6}\delta_j^y)}, \tag{2.8}$$

where $\delta_j^y = (\Delta\eta)^2(\partial^3 y/\partial\eta^3)_j/(\partial y/\partial\eta)_j$ is important when we have large grid variation. The second difference operator is obtained by recursion of (2.8). The above difference approximation has a truncation error $O(\Delta\eta^2)$ for arbitrary mesh transformation in problems of boundary-layer character.

In a study of non-uniform finite difference grids, it was found by Chenoweth & Paolucci (1981) that in order to compute the wall gradients accurately, the Roberts (1970) transformation

$$\left.\begin{aligned} \frac{\partial y}{\partial \eta} &= \tfrac{1}{2}AH_y(1 - L_y^2\,\tilde{y}^2), \\ H_y &= L_y^{-1}\tanh^{-1}L_y, \\ L_y &= (1 - S_y)^{\frac{1}{2}}, \end{aligned}\right\} \tag{2.9}$$

where $\tilde{y} = 2y/A - 1$, gives best results. The values of H_y and L_y are obtained by applying the constraints $\eta = 0$ and 1 at $y = \frac{1}{2}A$ and A respectively, along with the definition

$$S_y = \left(\frac{\partial y}{\partial \eta}\right)_{\eta=1} \Big/ \left(\frac{\partial y}{\partial \eta}\right)_{\eta=0}, \tag{2.10}$$

which represents a measure of grid reduction. With this transformation we then have that

$$\delta_j^y = 2(H_y L_y \Delta\eta)_j^2\,(3L_y^2\,\tilde{y}^2 - 1)_j. \tag{2.11}$$

S_y is a parameter that we choose which approximately represents the ratio between the smallest grid located at the wall to the largest grid located in the centre of the cavity. We typically choose values in the range $10^{-2} \leqslant S_y \leqslant 1$, where the upper bound represents a uniform distribution. Respective equations for the x-direction are obtained from (2.8)–(2.11) by letting $y \to x$, $\eta \to \xi$, and $A \to 1$.

Time advancement may be done either implicitly or explicitly. The first-order Euler explicit scheme was chosen since it was easy to implement, has a much lower computational cost per timestep, and requires much less computer memory allocation than an equivalent implicit implementation. We find that the first-order scheme was sufficiently accurate to resolve the smallest physical timescale. The stability of the scheme was found to be governed by the small grid spacing normal to the walls when non-uniform grids were used. This timestep was smaller than that required to resolve the largest frequency present in the flow. The finite-difference equations are solved using a predictor–corrector scheme (see Chenoweth & Paolucci 1986).

Finite-difference approximations of the nonlinear terms contain aliasing errors. These errors are usually less severe than corresponding ones obtained using spectral methods due to the damping at high wavenumbers of the difference approximation. Furthermore, these errors usually increase with the order of accuracy of the difference schemes. Lilly (1965) demonstrated that the staggered-mesh difference scheme used above preserves invariance properties of the original differential

$A = \frac{1}{2}$			
M	Ra	f_i	f_w
61×41	10^4	(7.50)	—
61×41	10^5	(22.25)	—
81×61	10^6	(74.74)	—
101×61	10^7	(229.4)	—
101×61†	10^8	(757.6)	—
101†	1.5×10^9	(1545)	(26100)
101†	1.7×10^9	(769.2)	(28370)
101†	1.8×10^9	278.0	29500
101†	1.9×10^9	295.7	30700
101†	2.0×10^9	315.6	31910
101†	2.5×10^9	2617	37680

$A = 1$			
M	Ra	f_i	f_w
61	10^4	(9.346)	—
61	10^5	(27.66)	—
81	10^6	(88.56)	—
81†	10^7	(273.3)	—
101†	4×10^7	(508.5)	—
121†	8×10^7	(747.7)	—
121†	10^8	(898.2)	—
121†	1.5×10^8	(1156)	(5447)
121†	1.75×10^8	(1197)	(6120)
121†	1.9×10^8	(621.0)	(6481)
121†	2×10^8	630.3	(6829)
121†	3×10^8	737.7	8856
121†	4×10^8	850.2	10770
121†	10^9	1215	28000
121†	10^{10}	11650‡	90300‡

$A = 2$			
M	Ra	f_i	f_w
81	10^6	(82.19)	—
121	2×10^7	(368.6)	(1400)
121	3×10^7	173.2	(1844)
121	4×10^7	70.07	2233
121	2×10^8	407.7	6367

$A = 3$			
M	Ra	f_i	f_w
61	10^5	(22.22)	—
81	10^6	(69.77)	—
101	5×10^6	(71.43)	(569.9)
101	7×10^6	(74.89)	730.8
101	10^7	40.32	922.2
101	5×10^7	126.1	2529
101	2×10^8	538.3	6112

† To obtain enough resolution we used: $A = \frac{1}{2}$: $S_x = S_y = 0.3$ for $Ra = 10^8$ and $S_x = 0.05, S_y = 1.0$ for $Ra = (1.5 \times 10^9, 2.5 \times 10^9)$; $A = 1$: $S_x = S_y = 0.3$ for $Ra = (10^7, 4 \times 10^8)$ and $S_x = S_y = 0.01$ for $Ra = (10^9, 10^{10})$.

‡ We also observed substantial energy at $f_i = 8000$ in the centre of the cavity, and $f_w = 30420$ in the vertical wall boundary layers.

TABLE 1. Fundamental frequencies resulting from the given aspect ratio and Rayleigh number value. M denotes the number of grids used in the computation; where one value is shown, that value is the same in both directions. Except as noted, all computations were performed with a uniform grid, i.e. $S_x = S_y = 1.0$. f_i and f_w represent fundamental frequencies of internal and wall waves, respectively; values in parentheses are observed during the transient approach to stationary flow, but eventually disappear.

equations such as conservation of mass, momentum, energy and circulation. Aliasing errors can violate these invariance properties and lead to nonlinear numerical instabilities. Thus it is felt that using a staggered mesh with second-order spatial accuracy, a first-order explicit time integration, accompanied by grids and timesteps small enough to resolve the small spatial and time scales would give us sufficiently accurate solutions.

The computations were performed with a number of grids which varied with aspect ratio and Rayleigh number as given in table 1. Note that when a single number is given in the table, it implies that the number was the same in both directions, and when two numbers are given, the second represents the number of grid points used in the vertical direction. Many of the calculations were obtained using different spatial resolution (different number of grids or different S_x and S_y) without much apparent change in the results.

For a detailed description of the computational procedure, including validation and accuracy of the computer program, the reader is referred to Chenoweth & Paolucci (1986).

2.3. *Statistical analysis*

Long-time simulations, following the initial transients in the time evolution, serve as the basis for statistical analysis. In all cases the asymptotic time dependent solution is obtained by letting the integration time be long enough so that all frequencies reported were stationary to within 1%. We do note, however, that at the same time the first and second moments of temperature and velocity at the selected locations were typically stationary to within 1% and 5% respectively in regions where the highest frequency dominates, and to within 5% and 20% respectively in regions where the lowest frequency dominates. Thus the flow is considered to be approximately stationary to second order. The largest errors in the statistics resulted from simulations which led to a steady-state. In those cases the unsteady approach was so rapid that only a limited time series was available.

The critical Rayleigh number for the onset of an oscillatory instability is determined indirectly for the different aspect ratios. The time records for the temperature and velocity components at selected points are obtained for different Rayleigh numbers. The initial condition used causes disturbances to be amplified or damped depending on the Rayleigh number being above or below the critical value. By performing sufficient calculations the critical value can be bounded and approximately determined.

A number of experiments (cf. Fenstermacher *et al.* 1979; Gorman & Swinney 1982; Gollub & Benson 1980) have shown that periodic flow is the first step in a sequence of instabilities. By increasing the Rayleigh number we examine the additional instabilities obtained by the numerical simulation. Different dynamical regimes of the flow can be distinguished by examining high-resolution power spectra of the fluctuating values of velocity and temperature at fixed locations. Transitions that are obvious in the power spectra, such as the appearance of a new characteristic frequency in the flow, can sometimes go undetected in a direct inspection of the time records or flow fields. Furthermore, they may not even appear in the power spectra if the probed location is not relatively close to the source of instability. Thus power spectra can be a major tool for the study of the transition from laminar to turbulent flow when obtained at properly selected locations. Power spectra are computed from the squared modulus of the fast Fourier transform of T, u and v using standard discrete techniques and processed with the Hann window (see Otnes & Enochson 1978). Spectral estimates are obtained at frequency intervals of $1/\mathscr{T} = 1/N\Delta t$ up to the Nyquist frequency $f_N = 1/2\Delta t$. The resolution of the computed spectra is approximately equal to the interval $1/\mathscr{T}$ between spectral estimates. Because both high resolution and a broad spectral range are needed to distinguish between the different dynamical regimes of a flow, data records should contain as many samples as possible. Typical records consist of N between 1000 to 10000 sequential samples with a frequency resolution $\Delta f/f_N$ of the order of 10^{-3}–10^{-4}. Thus changes in the dynamics of the flow can be detected with high sensitivity. We note that in the following figures, only a small fraction of the complete records are shown.

Although not presented here, we note that the behaviour of the local heat transfer on the sidewalls mirrors that of the adjacent temperature field. However, even though the character of the *average* heat transfer on the sidewalls is consistent with that of the global flow field, one must be careful in interpreting the actual frequencies obtained from such data alone.

3. Results

It has become a generally accepted fact that the first transition to turbulence in the differentially heated cavity occurs by instability of the boundary layers on the vertical walls. This has been shown to be the case in a number of experimental works (e.g. Eckert & Carlson 1961; Mordchelles-Regnier & Kaplan 1963; Elder 1965) and more recently in the numerical works of Le Quere & Alziary de Roquefort (1985*a*, 1985*b*, 1986). The one characteristic that all the above studies have in common is that primarily aspect ratios substantially larger than unity were investigated. However, experimental observations of the oscillatory approach to steady-state by Ivey (1984) for $Pr = 7.1$ and sufficiently large Ra, clearly indicated that the oscillations for $A = 1$ are due to wave-breaking arising from internal 'hydraulic' jumps near the departing corners.

It will be shown below that for aspect ratios near unity, as the Rayleigh number is increased an oscillatory instability due to internal waves occurs before the wall boundary layers become unstable (this was first pointed out by Chenoweth & Paolucci 1986). We know of no other result which shows that this first transition to time dependent flow is due to an internal wave instability. This strictly periodic time dependence evolves from a steady flow and is recognized by a periodic solution showing sharp peaks in the power spectrum and these peaks are harmonics of a single fundamental frequency f_i. This is followed by a quasi-periodic (or doubly periodic) state displaying sharp peaks containing two incommensurate frequencies f_i and f_w, along with linear combinations of these fundamental frequencies. As the Rayleigh number is further increased, broadband components appear in the spectra in addition to the narrow peaks. This non-periodic flow is regarded as being weakly turbulent, since it appears from the flow fields that the flow varies randomly in space as well as in time. This flow has properties of both periodic and turbulent flows: the narrow peaks indicate that the velocity correlations persist, yet the broad components clearly indicate a chaotic element in the flow.

3.1. *Transition to unsteady flow*

As a result of the numerous computations for various values of A and Ra listed in table 1, we obtain the stability map displayed in figure 1. This figure is a more detailed and accurate stability map of the lower right corner of figure 3 given in Chenoweth & Paolucci (1986). The solid and dashed lines in the figure represent the critical Rayleigh numbers Ra_i for internal waves and Ra_w for the wall boundary layers, respectively. To the left of the curves perturbations are damped while to the right they are amplified leading to oscillatory flow. From the figure it is evident that for $\frac{1}{2} < A < 3$ the internal waves become unstable before the wall boundary layers. It is also evident that the change in slope of the neutral stability curve for the wall boundary layers near $A = 3$ is due to an interaction between the boundary layers and internal waves near the departing corners. This point is illustrated in figure 2 where the streamlines for $Ra = 5 \times 10^6$ and $A = 3$, and $Ra = 10^6$ and $A = 5$ are shown. The vertical wall boundary layers first become unstable near the end regions and it is there that the presence of the stationary internal jumps and their interaction with the boundary layers occur. From the steady streamlines in figure 2(*a*) we see that the presence of the opposite walls constains and indeed damps the downwstream oscillations of the internal jumps to such an extent that for significantly larger aspect ratios, as can be seen in figure 2(*b*), stationary jumps cannot develop at all near Ra_w. We note that in figure 2(*b*) the boundary layers are unsteady, but the amplitude

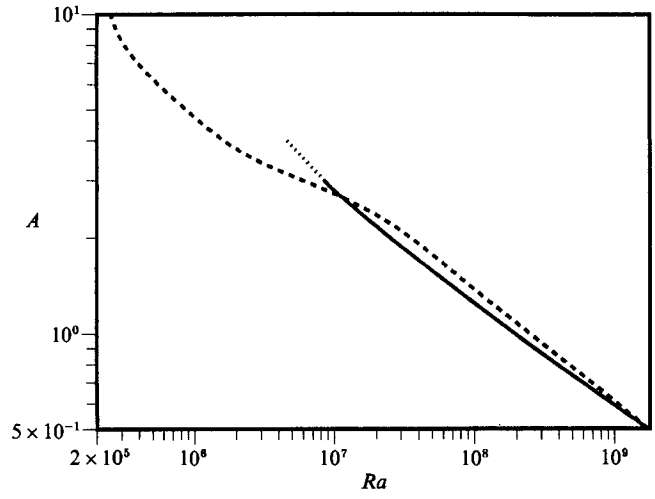

FIGURE 1. Critical Rayleigh numbers as functions of aspect ratio: ——, Ra_i; – – – –, Ra_w.

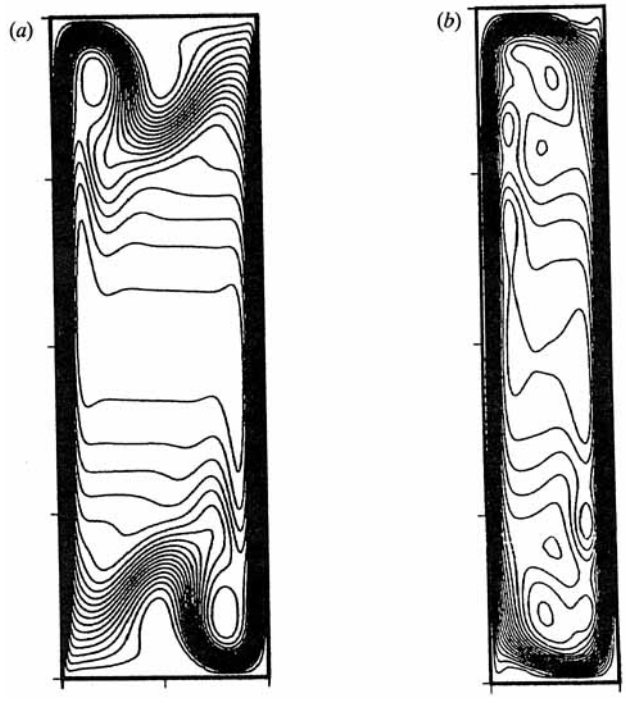

FIGURE 2. Stream fields: (a) $A = 3$ and $Ra = 5\times10^6$; (b) $A = 5$ and $Ra = 10^6$.

of the oscillations are imperceptible in the figure. In the range $\frac{1}{2} < A < 2$ the curves in figure 1 are described to a good approximation by

$$Ra_i = 1.93\times10^8 A^{-3.15}, \tag{3.1}$$

and

$$Ra_w = 2.70\times10^8 A^{-2.75}. \tag{3.2}$$

We now show that (3.1) and (3.2) are consistent with estimates obtained by the use of simple arguments and previous analyses.

3.1.1. *Internal wave instability*

Using reasoning similar to Patterson & Imberger (1980) and Ivey (1984) but for a fluid with $Pr < 1$, we consider the corner region where the rising (falling) flow is turned due to the presence of the top (bottom) boundary. For values of A, Ra, and Pr in the steady boundary-layer regime, if we compute the average vertical velocity $\bar{v}$ and momentum thickness δ_v at the midheight of the cavity, we find that $\bar{v}/v_{\mathrm{M}} = \delta_v/\delta = 0.497$, where v_{M} is the maximum vertical velocity and δ is the boundary-layer thickness. If we further assume constant pressure in the corner regions, from conservation of mass (using results of Chenoweth & Paolucci 1986) we can write

$$\bar{u} = 0.1298(A\,Pr\,Ra)^{\frac{1}{2}}, \tag{3.3}$$

and

$$\Delta = 2.145\left(\frac{A}{Pr\,Ra}\right)^{\frac{1}{4}}, \tag{3.4}$$

where $\bar{u}$ is the average horizontal velocity and Δ is the local momentum thickness of the intrusion, or wall jet. Now, following Ivey (1984), a characteristic internal Froude number can be defined for this horizontal flow by

$$Fr = \frac{\bar{u}}{(g'\Delta)^{\frac{1}{2}}}, \tag{3.5}$$

where $g' = \frac{1}{2}Pr\,Ra$. Using (3.3) and (3.4), and their equivalent for $Pr > 1$, in (3.5) we obtained the result

$$Fr = \begin{cases} 0.125A^{\frac{3}{8}}(Pr\,Ra)^{\frac{1}{8}} & \text{if } Pr \leqslant 1, \\ 0.125A^{\frac{3}{8}}Pr^{-\frac{1}{2}}Ra^{\frac{1}{8}} & \text{if } Pr > 1. \end{cases} \tag{3.6}$$

The flow is critical when $Fr = 1$ (see Ivey 1984; Turner 1973). If the flow is subcritical ($Fr < 1$), it spreads out smoothly over (under) the heavier (lighter) fluid as the intrusion approaches the cold (hot) wall. If the flow is supercritical ($Fr > 1$) the flow may undergo an internal 'hydraulic' jump. As pointed out by Ivey (1984), by analogy with open-channel flow (Lighthill 1978), the energy loss associated with any internal jump is dissipated in a stationary wavetrain downstream of the jump for $1 < Fr < 1.3$, but for higher values of Froude numbers, these waves break, resulting in an unsteady wave downstream. Indeed from (3.6), for $Pr \leqslant 1$ we see that steady jumps should become apparent at

$$Ra > \widehat{Ra}_{\mathrm{s}} = \frac{1.65 \times 10^7}{Pr\,A^3}, \tag{3.7}$$

and unsteady (and eventually disordered) for

$$Ra > \widehat{Ra}_{\mathrm{i}} = \frac{1.34 \times 10^8}{Pr\,A^3}. \tag{3.8}$$

The last estimate is in good agreement with the simple numerical correlation (3.1). Furthermore, the above scenario is in qualitative agreement with the corner flow regions of $A = 1$ displayed in figure 3 (*a–d*) for increasing values of Ra. In the figures all values of the Froude number are supercritical (1.30, 1.31, 1.37 and 1.42 for figures 3 (*a–d*) respectively), but only the flow field in figure 3 (*a*) is steady. Notice that the flows are symmetric in figures 3 (*a*) and (*c*) but not in 3 (*b*) and (*d*). This anomaly and the connection with the frequencies present in the flow are discussed later. The above description is consistent with the limited computational results of Haldenwang

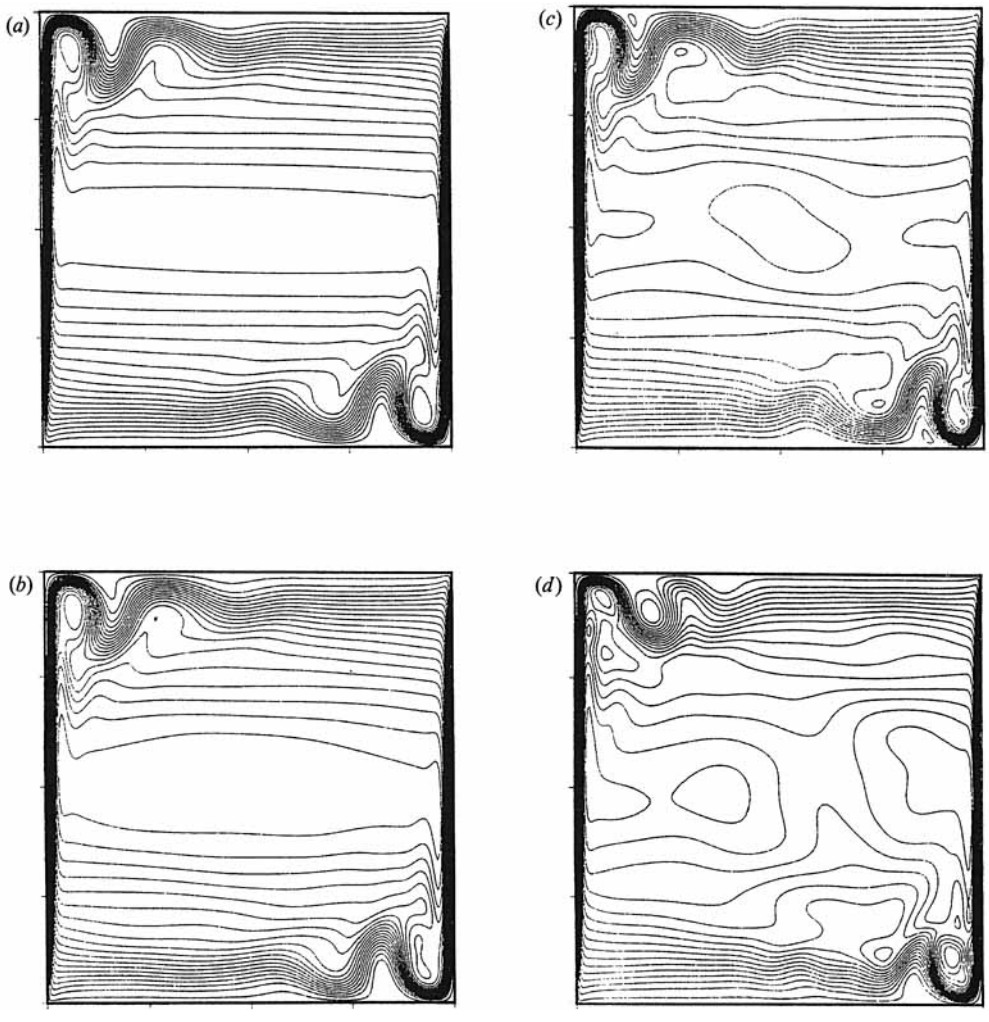

FIGURE 3. Stream fields for $A = 1$: (a) $Ra = 1.9 \times 10^8$; (b) $Ra = 2.0 \times 10^8$; (c) $Ra = 3.0 \times 10^8$; (d) $Ra = 4.0 \times 10^8$.

(1986) who shows that for $A = 1$ the flow becomes unsteady for Ra between 10^8 and $10^{8.5}$. In addition, for $A = 1$, $\widehat{Ra}_s$ is consistent with the numerical results of Le Quere & Alziary de Roquefort (1985*a*), Chenoweth & Paolucci (1986) and Haldenwang (1986), who find the appearance of recirculating regions near the departing corners at Ra within the ranges 10^7–4×10^7, 10^7–4×10^7, and 10^7–$10^{7.5}$, respectively. The internal jumps are identified by the steep large-amplitude waves and distinct recirculating regions on the horizontal walls.

The only relevant experimental results are those of Ivey (1984). While the structures and associated eddies disappeared in Ivey's experiment as the flow evolved to steady state, in our computations they persist and give rise to the oscillatory instability. To clarify that this difference is strictly due to a Prandtl number dependence, we performed a simulation starting from quiescent conditions for $A = 1$ with $Pr = 7.1$ and $Ra = 9.2 \times 10^8$, which corresponds to one of Ivey's test cases. The resulting flow fields are similar to those of Ivey for the time range reported by him. Our respective temperature traces at the same two probe locations are

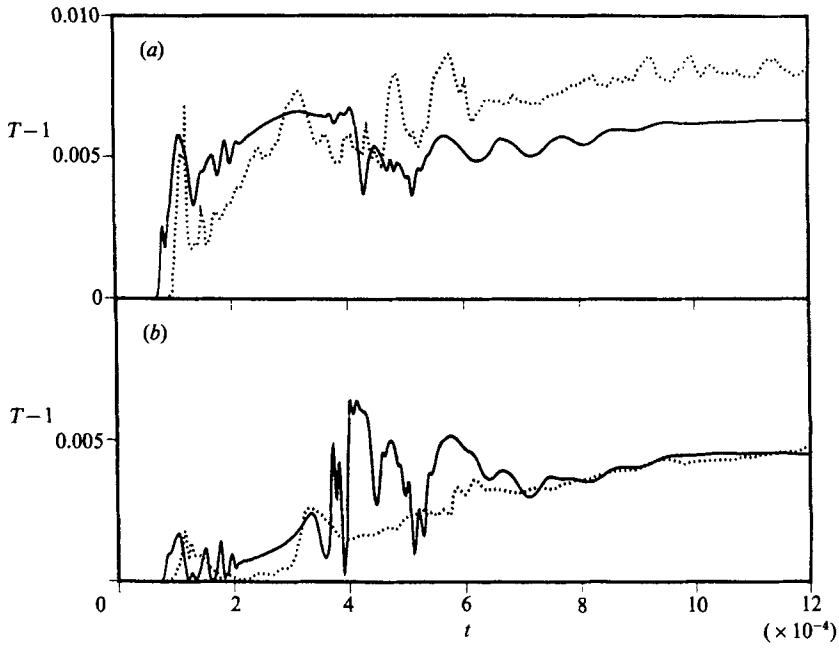

FIGURE 4. Time histories of $T-1$ for $A = 1$, $Pr = 7.1$ and $Ra = 9.2 \times 10^8$ at locations: (*a*) $x_i = (0.21, 0.967)$; (*b*) $x_i = (0.21, 0.937)$. The solid lines are from our simulation, while the dotted ones are from Ivey's (1984) experiment.

displayed in figure 4(*a*, *b*). We observe that the time responses are surprisingly similar considering the fact that the probed locations are unfortunately located very close to the top boundary where small experimental heat losses greatly affect the location of the existing structures relative to those of the probes. We note that while it appears that the flow is proceeding to a steady state, in fact we find that the wall boundary layers become unsteady and remain oscillatory long after the internal waves have decayed. This instability only becomes evident for $t > 2 \times 10^{-3}$, which is substantially later than the last time reported by Ivey. Since in this particular case $Fr = 0.62$ (from 3.6)) and $Ra > \widehat{Ra}_w = 2.2 \times 10^8$ (see (3.9)), then the simulation results are also consistent with the stability estimates.

In figure 5(*a–d*) we show similar flow fields for $A = 2$. In this case from (3.6) we have $Fr = 0.87$ in 5(*a*), 1.27 in 5(*b*), 1.34 in 5(*c*), and 1.39 in 5(*d*). We note that the flows in figures 5(*a*) and 5(*b*) are steady, while figures 5(*c*) and 5(*d*) represent snapshots of time dependent flows. The presence of a jump is evident in figure 5(*b*) while the loss of symmetry is apparent in 5(*d*). The loss of symmetry, as is discussed later, appears to be due to the fact that the flow is quasi-periodic with two incommensurate fundamental frequencies present, one due to oscillatory internal waves, the other to the unstable wall boundary layers. This behaviour is also observed even during the approach to statistical steady state when both frequencies are present. However, we do not know any physical reason why this spatial and temporal symmetry breaking should occur simultaneously. When only one frequency is present, either during the transient or at statistical steady state, the flow retains the symmetry imposed by the data. Indeed in figure 5(*c*) only one fundamental frequency due to the instability of internal waves is present as shown in figure 6. Figure 6(*a*) is a time record of $T-1$ obtained at $x_i = (3.554 \times 10^{-1}, 1.645)$. Figures

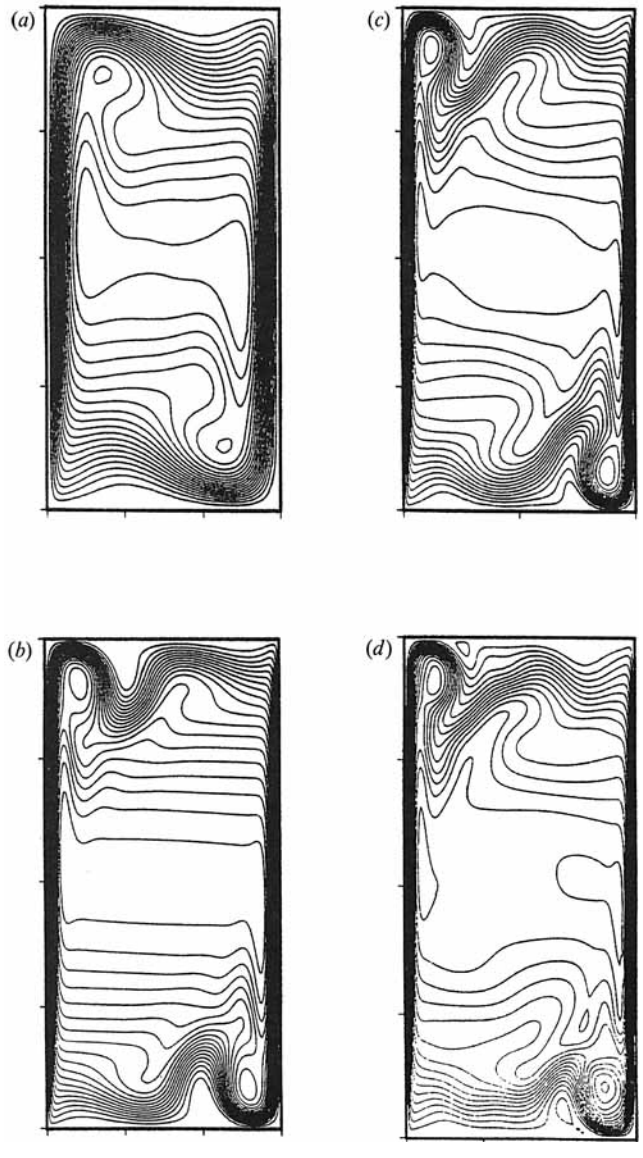

FIGURE 5. Stream fields for $A = 2$: (*a*) $Ra = 10^6$; (*b*) $Ra = 2 \times 10^7$; (*c*) $Ra = 3 \times 10^7$; (*d*) $Ra = 4 \times 10^7$.

6(*b*)–6(*d*) are the responses of $T-1$, u and v, respectively, shown on expanded timescales. Some information about the spatial structure of this oscillatory flow can be obtained by looking at the flow fields shown in figures 5(*c*) and 7 which correspond to the specific times through the period labelled (i)–(v) in figures 6(*b*)–6(*d*). As readily observable, the flow field in 7(*d*) is essentially the same as that in 5(*c*). The primary reason for the small differences is that the two times (i) and (v) are not exactly one period apart. As seen from the figures, the cycle begins with the large-amplitude waves retracted against the vertical walls in figure 5(*c*); they collapse and at the same time move away from the walls in figure 7(*a*); the separated regions begin to grow again as the waves continue to move forward in figure 7(*b*); they reach their

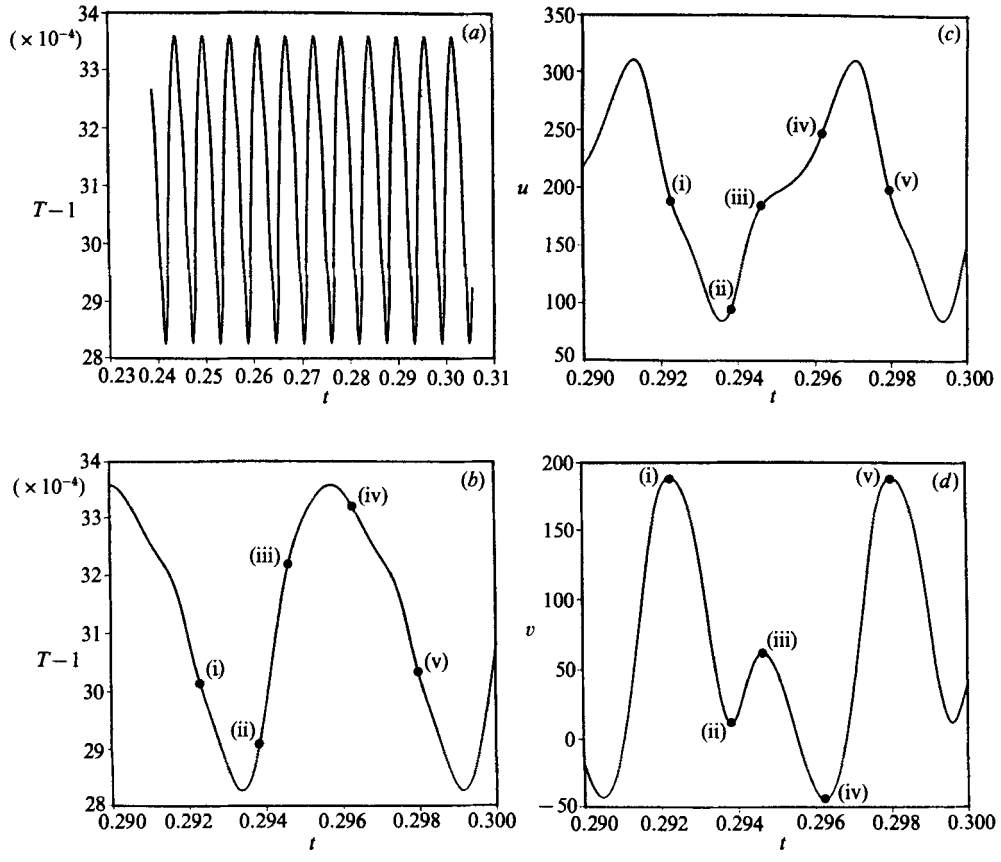

FIGURE 6. Time histories for $A = 2$ and $Ra = 3 \times 10^7$ obtained at $x_i = (3.554 \times 10^{-1}, 1.645)$: (*a*) $T-1$; (*b*) $T-1$; (*c*) u; (*d*) v. The symbols (i)–(v) correspond to values of time at which stream fields are given in figures 5(*c*), and 7(*a*)–(*d*), respectively.

maximum extent and amplitude in figure 7(*c*); and finally they recoil back against the vertical walls in figure 7(*d*) to complete the cycle. The frequency of this oscillation is f_1.

3.1.2. *Boundary layer instability*

Using existing linear stability results, we can further obtain an analytical estimate of Ra_w given in figure 1 and approximated by (3.2). The stability of the wall boundary layers is very closely related to that of the buoyancy layer studied by Gill & Davey (1969) and Bergholtz (1978) since an approximately constant vertical density gradient is present in the core of the cavity. It can be shown that the thermal stratification parameter $(A/\Delta T)\,(\partial T/\partial y)_{x=\frac{1}{2}}$ is typically close to unity in this region of parameter space (see also Chenoweth & Paolucci 1986). Using a value of unity in conjunction with the buoyancy-layer stability results, we get that

$$\widehat{Ra}_w = 4(RPr)^4 A^{-3}, \tag{3.9}$$

where $\hat{R}$ depends on the Prandtl number as shown in table 2 which has been adapted from table 1 of Gill & Davey (1969). The aspect ratio dependence of A^{-3} is in good agreement with that given by (3.2). The larger discrepancy between the coefficient of 1.13×10^8 given by (3.9) for $Pr = 0.71$ and that in (3.2) can be attributed to

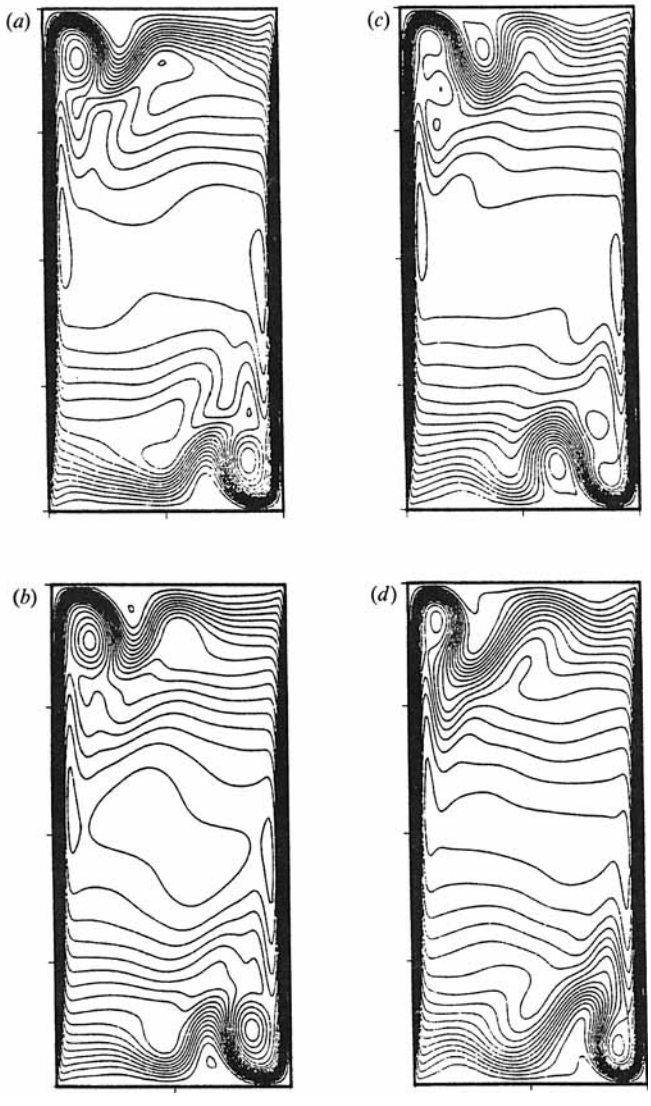

FIGURE 7. Stream fields for $A = 2$ and $Ra = 3 \times 10^7$: (a)–(d) correspond to time values (ii)–(v) in figure 6.

interactions with the internal waves. Nevertheless, the dashed curve for $A \geqslant 4$ in figure 1 and (3.9) are in excellent agreement with Elder's (1965) experimental estimate using water, and the results reported in table 1 of Le Quere & Alziary de Roquefort (1986) for $Pr = 0.71$. Note that the Prandtl number dependence in (3.9) is weak at Prandtl numbers of order unity, while it approaches the limit of Pr^2 as $Pr \to \infty$. The good agreement between our results and equation (3.9) is surprising in light of the fact that from the stability analyses it can be shown that the critical wavelength is given by

$$\lambda_c = \frac{2\pi}{\hat{\alpha}\hat{R}}\left(\frac{A}{Pr}\right), \tag{3.10}$$

where $\hat{\alpha}$ is given in table 2. For $Pr = 0.71$ we obtain $\lambda_c \approx 0.3A$, which would put into question the applicability of the buoyancy-layer results to finite cavities at low

Pr	$Pr^{\frac{1}{2}}\hat{R}$	$\hat{\alpha}$	$\hat{c}$
0.72	85.9	0.289	0.281
1	76.1	0.278	0.313
2	53.6	0.326	0.347
4	38.3	0.381	0.375
10	26.9	0.436	0.409
20	22.1	0.458	0.432
50	18.5	0.465	0.456
100	17.0	0.463	0.471
200	16.2	0.454	0.482
400	15.9	0.445	0.491
∞	15.0	0.417	0.512

TABLE 2. Critical values of $\hat{R}$, $\hat{\alpha}$, and $\hat{c}$, as functions of Prandtl number Pr

Prandtl numbers. We note that (3.10) is only valid when $A < \hat{R}Pr/10$, since it is only then that the boundary layers in the cavity become thin enough to make any comparison to the buoyancy-layer limit relevant.

3.2. *Time series and frequency spectra*

A comparison of different power spectra shows that a frequency observed at an arbitrary point can be detected in the spectra of all variables in the flow field, provided that the Rayleigh number is well above the critical value and that the resolution of the spectral analysis sufficient. However, the amplitude of a certain frequency depends strongly on the variable considered and on the location of the measurement.

This is illustrated for $A = 2$ and $Ra = 3 \times 10^7$ in figure 8, where power spectra for $T-1$, u and v are displayed. The spectra are based on the same time interval, a small part of which is shown in figure 6(a), at a location near the internal jump. As evident from figure 8 (and table 1), the spectra all show the same fundamental frequency of 173.2 and several higher harmonics that are integral multiples of the fundamental. Similarly, time samples and spectra for $T-1$ at two boundary-layer locations and in the centre of the cavity are shown in figure 9(a–c) using the same coordinate scales as in figures 6(a) and 8(a). In the figures we also display enlargements of the time samples showing the detailed structure of the oscillations. The figures show the striking attenuation of the temperature oscillations with increasing distance from the departing corner. We note that even though the fundamental frequency can be detected by looking at the time records, in some of the cases its power content is too small to appear within the five orders of magnitude shown. This example demonstrates that unless one can isolate the source of the instability, it is difficult to characterize the flow field by one single power spectrum recorded at one fixed point. The amplitudes of the different peaks in a power spectrum are not representative for the global flow field but depend on the spatial location. The figures do show that the amplitudes are largest in the corner region and decrease as we approach the centre of the cavity as well as the vertical walls, thus clearly indicating that the source of instability is the internal jump. The wall boundary layers were also observed to be unstable during the transient but their oscillations damped as the flow became stationary. In table 1 we report the observed fundamental frequencies for damped (in parentheses) and undamped oscillations for both internal wave and wall boundary-layer oscillations, f_i and f_w respectively, as the flow approached stationarity.

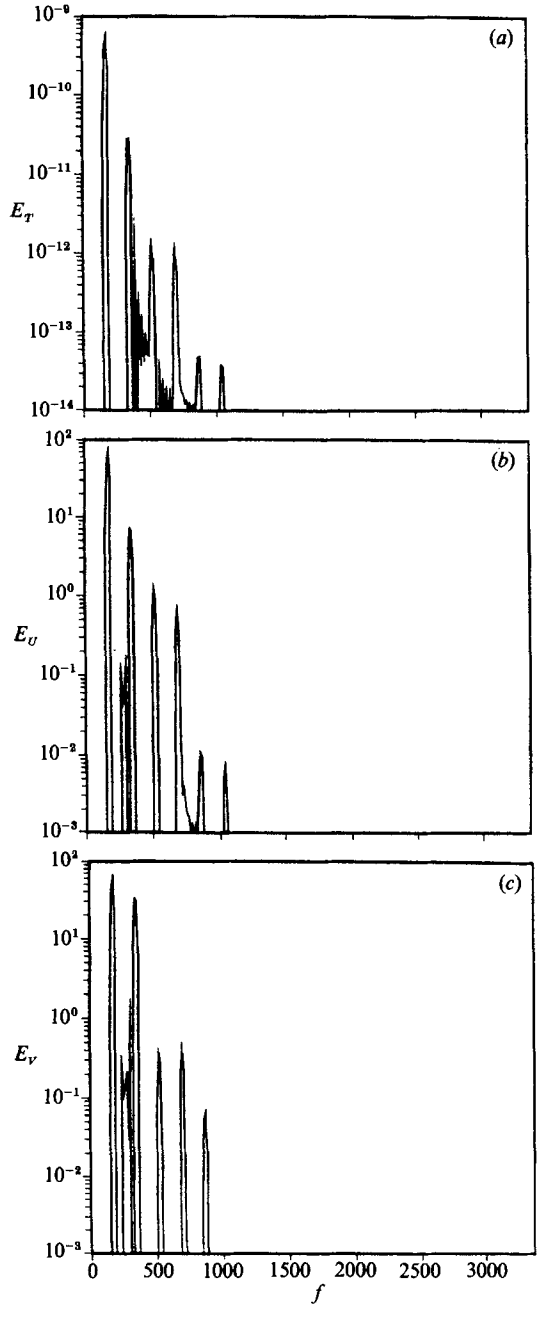

FIGURE 8. Power spectra for $A = 2$ and $Ra = 3 \times 10^7$ at $x_i = (3.554 \times 10^{-1}, 1.645)$: (*a*) E_T; (*b*) E_U; (*c*) E_V.

For $A \leqslant \frac{1}{2}$ and $A \geqslant 3$ the first instability is due to the wall boundary layers as Ra increases. Figure 10 shows typical time samples and spectra of $T-1$ for $A = 3$ and $Ra = 7 \times 10^6$. The steady flow for $Ra = 5 \times 10^6$ shown in figure 2(*a*) was used for initial conditions. By inspecting the amplitudes of the samples and spectra at the given locations it is clear that only one fundamental frequency exists and is

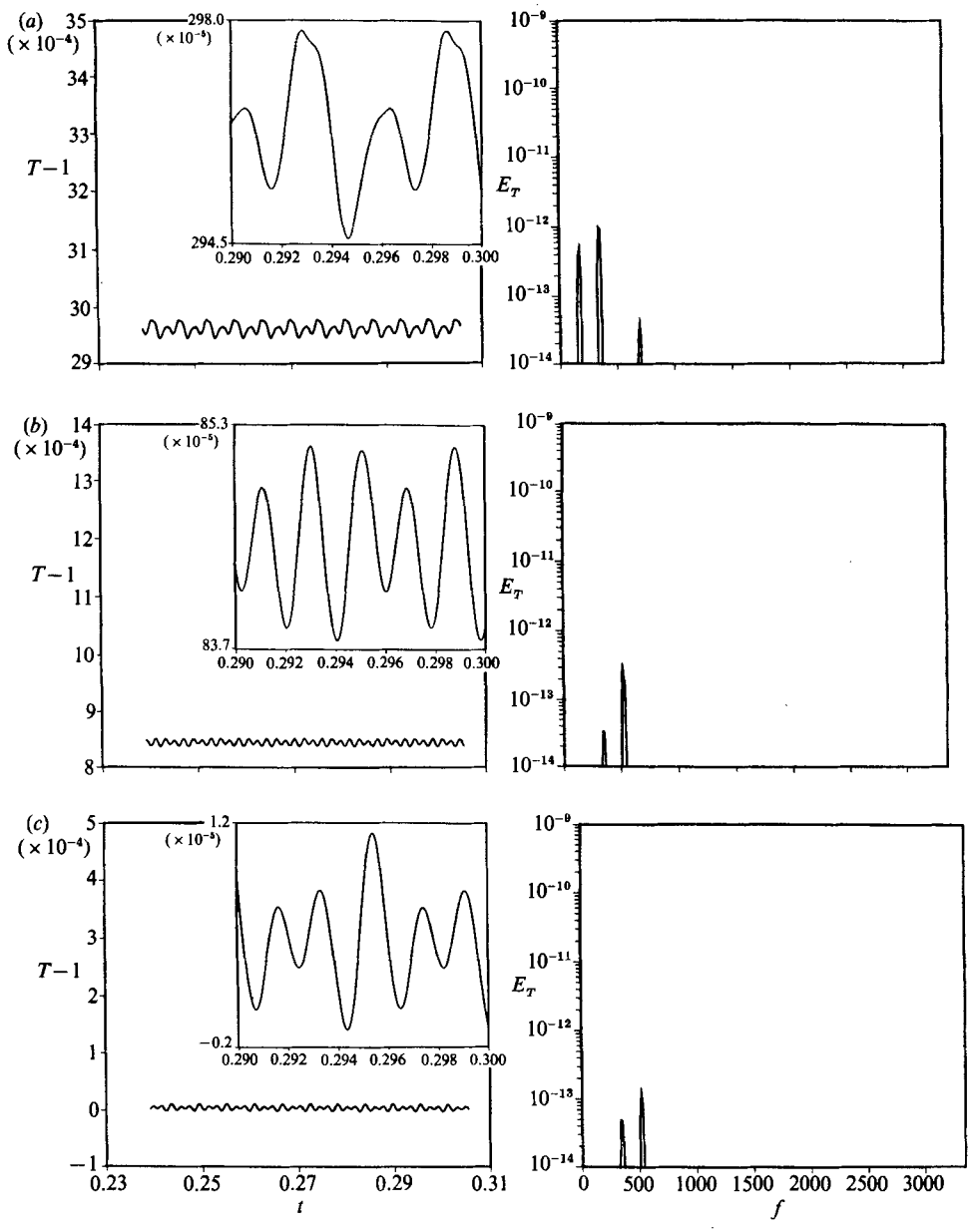

FIGURE 9. Time histories and power spectra at $T-1$ for $A = 2$ and $Ra = 3 \times 10^7$ at locations: (*a*) $x_i = (2.893 \times 10^{-2}, 1.645)$; (*b*) $x_i = (2.893 \times 10^{-2}, 1.0)$; (*c*) $x_i = (0.5, 1.0)$.

associated with the instability of the wall boundary layers. Note that remnants of the damping internal waves, even though having seven orders of magnitude less power, can still be seen in figure 10(*d*) obtained from the centre of the cavity. Furthermore, we note that the frequency of oscillations due to the boundary-layer instability is approximately one order of magnitude larger than that due to the damping internal waves, and as expected the higher frequency attenuates faster than the lower one in space as well as in time.

For aspect ratios $\frac{1}{2} < A < 3$ and Rayleigh numbers $Ra_i < Ra < Ra_w$, and $A \leqslant \frac{1}{2}$ or

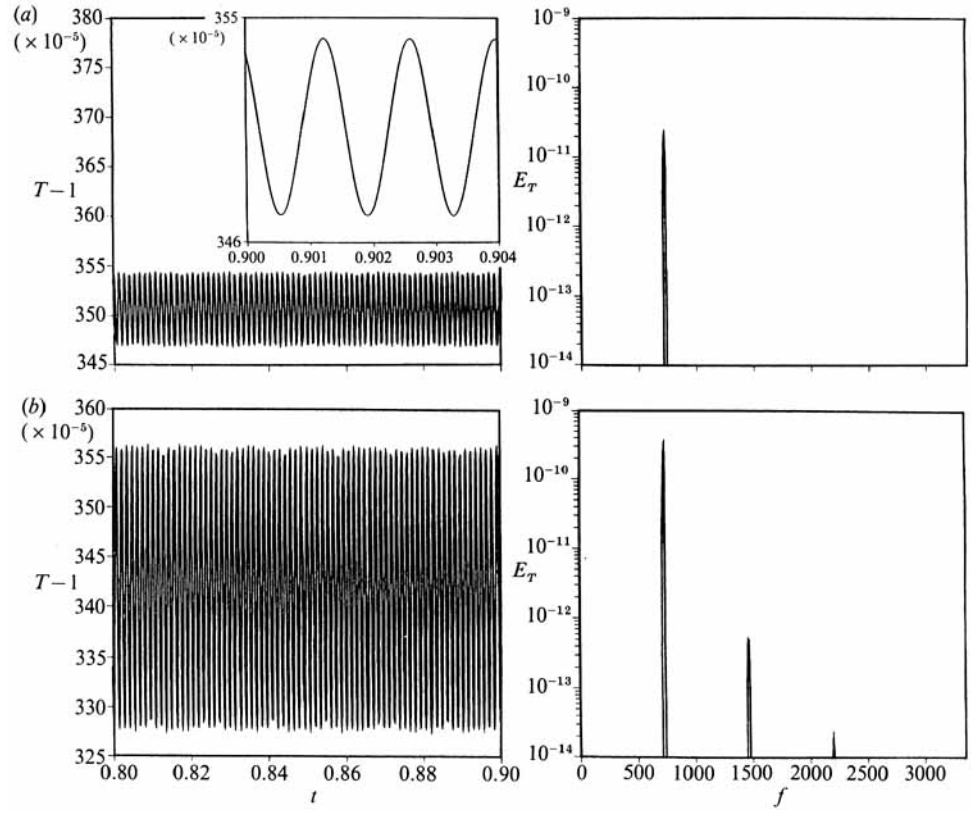

FIGURE 10(*a*, *b*). For caption see facing page.

$A \geqslant 3$ and $Ra_w < Ra < Ra_i$, the power spectra contained only a single frequency component f_i or f_w, respectively, and their related harmonics; hence the flow in those regions is strictly periodic. The same frequencies are observed at different positions in the flow fields, although the amplitudes of the spectral components varied with location. The extent of the range of aspect ratios below $\frac{1}{2}$ where the wall boundary layers become unstable first is not known at this time. For A larger than 3, Le Quere & Alziary de Roquefort (1986) have shown that this instability occurs for aspect ratios at least as large as 10.

In order to obtain more detailed information about the bifurcations, a number of calculations were made with $A = 1$ by varying the Rayleigh number in the vicinity of the bifurcation points. These calculations are not listed in table 1 since they were not carried through a long enough period of time past stationarity to obtain statistics from them. Since we compute the solutions from initial conditions and wait until the flow eventually equilibrates to its stable state, we necessarily compute only the physically stable branches of the bifurcation diagram. It is therefore difficult in general to identify the fact that a bifurcation has occurred. Our reasons for claiming that a bifurcation has occurred are that the equilibration times become much longer as we approach this point, the character of the solution changes dramatically at the point as evidenced by the power spectra, and the amplitudes of the spikes in the power spectra decrease to zero as the point is approached from above.

In figure 11 we show the amplitudes of $T-1$, u and v at $x_i = (1.032 \times 10^{-1}, 8.036 \times 10^{-1})$ for various Rayleigh numbers near the first critical point. From the

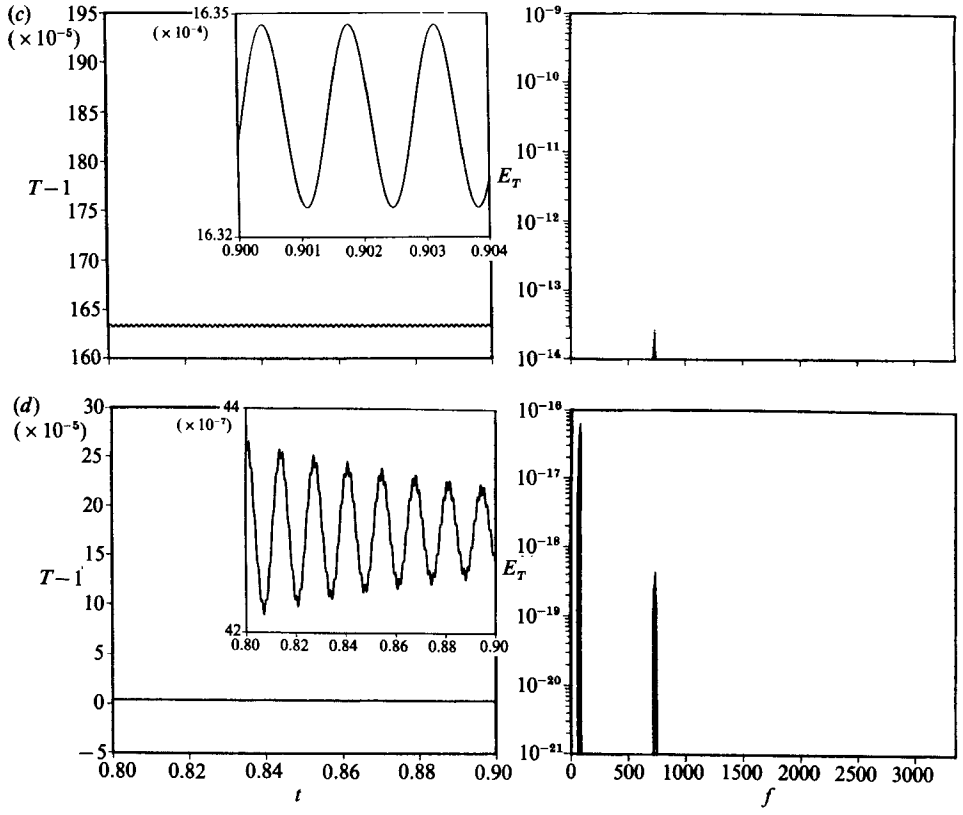

FIGURE 10. Time histories and power spectra of $T-1$ for $A = 3$ and $Ra = 7 \times 10^6$ at locations: (*a*) $x_i = (0.5, 2.510)$; (*b*) $x_i = (3.465 \times 10^{-2}, 2.510)$; (*c*) $x_i = (3.465 \times 10^{-2}, 1.5)$; (*d*) $x_i = (0.5, 1.5)$.

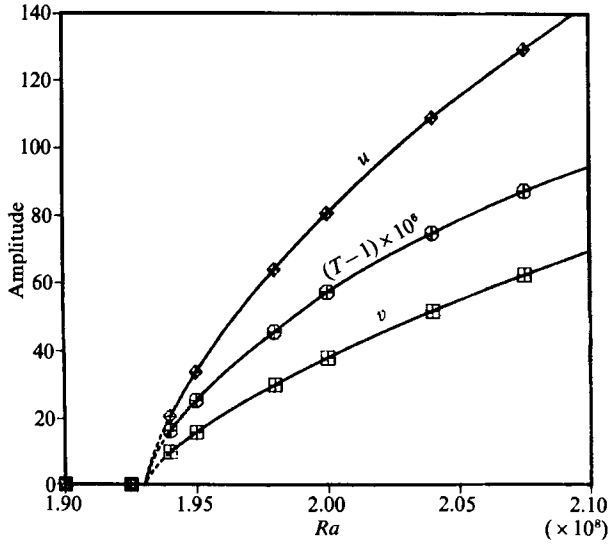

FIGURE 11. Bifurcation diagram of the first instability for $A = 1$ showing the maximum amplitudes of $T-1$, u and v.

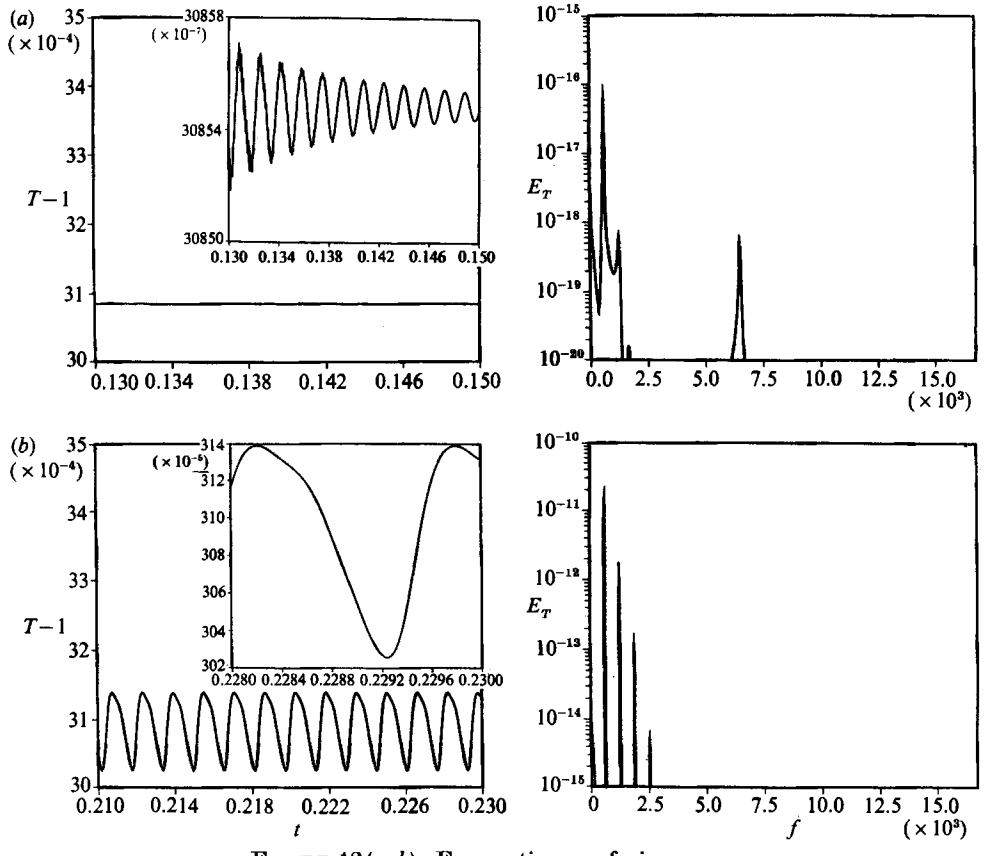

FIGURE 12(*a*, *b*). For caption see facing page.

results it appears that it is a classical Hopf bifurcation located near $Ra = 1.93 \times 10^8$. The non-existence of a hysteresis was verified by approaching the critical point from above and below. Similarly, Le Quere & Alziary de Roquefort (1986) have shown than when the wall boundary layers become unstable first, the critical point is also a Hopf bifurcation.

As the Rayleigh number is increased further we observe a second bifurcation to a quasi-periodic regime. We do know that this instability is due to the wall boundary layers. Furthermore, we have sufficient evidence indicating the presence of hysteresis near this critical point – the transition occurred at 2.7×10^8 with increasing and 2.55×10^8 with decreasing Rayleigh number. At aspect ratios larger than 3, Le Quere & Alziary de Roquefort (1986) have shown that instability of the wall boundary layers lead to a supercritical Hopf bifurcation. Our results would then indicate that for $A < 3$ the hysteresis is possibly due to the physical interaction of the two unstable mechanisms.

Somewhere within the Rayleigh number range of 3×10^8 to 4×10^8, as will be evident from results given below, the flow undergoes a further bifurcation to a chaotic flow.

Additional information regarding the instabilities is obtained by observing the variation of power spectra at the different Rayleigh numbers. In figure 12(*a–e*) we show the frequency spectra and portions of the corresponding time records of $T-1$ obtained at the same location as the above bifurcation diagram. We note that in all

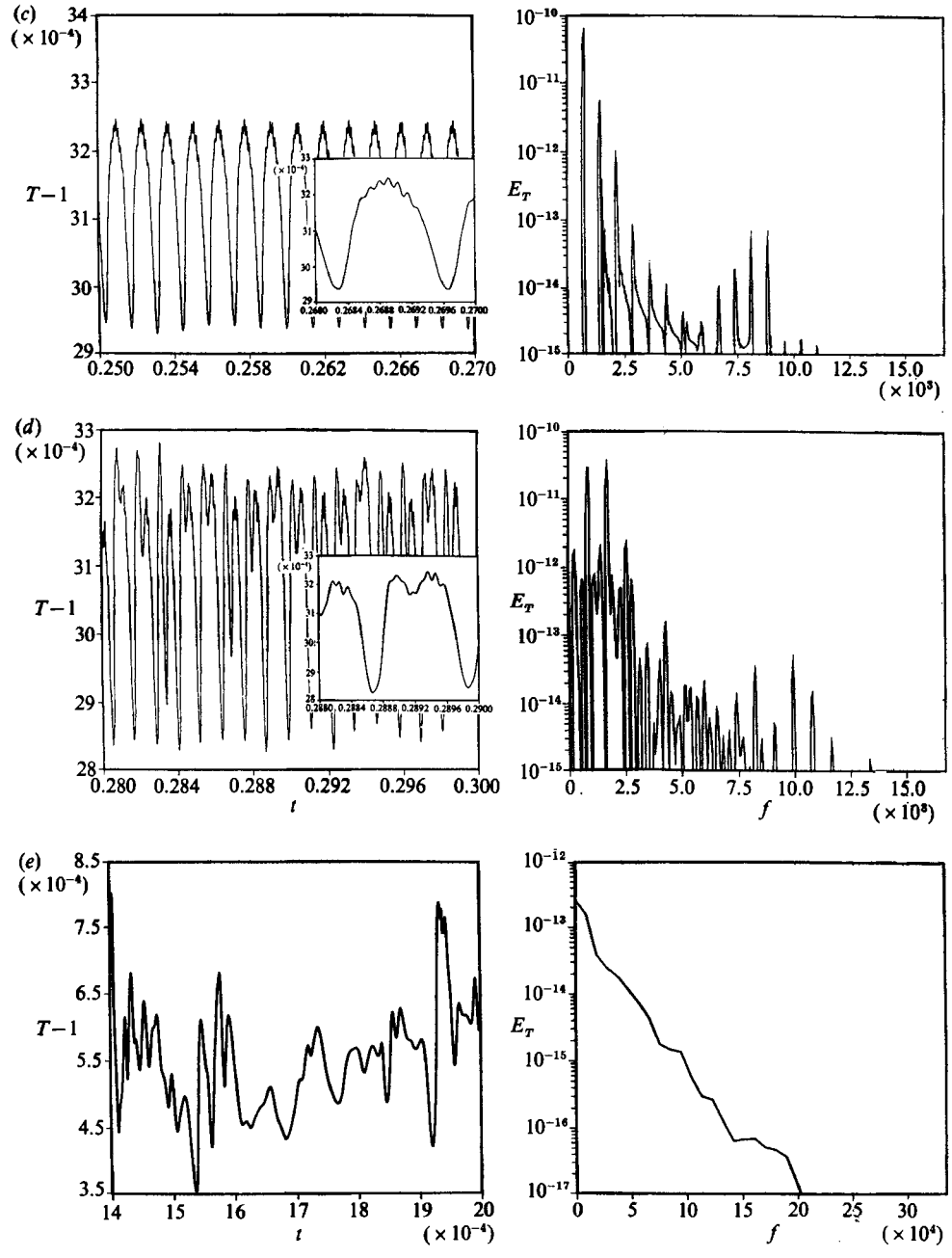

FIGURE 12. Time histories and power spectra of $T-1$ for $A = 1$ at the point $x_i = (1.032 \times 10^{-1}, 8.036 \times 10^{-1})$: (*a*) $Ra = 1.9 \times 10^8$; (*b*) $Ra = 2.0 \times 10^8$; (*c*) $Ra = 3.0 \times 10^8$; (*d*) $Ra = 4.0 \times 10^8$; (*e*) $Ra = 10^{10}$.

cases, except in figure 12(*e*), the time samples and frequency spectra are plotted on the same scales to make comparisons easier. To show the resolution of the time samples, details are also shown as insets. We further note that figures 3(*a*)–3(*d*) are snapshots of streamlines obtained within the sampled range used to obtain the spectra in figures 12(*a*)–12(*d*), respectively.

In figure 12(*a*) we easily see that the flow at $Ra = 1.9 \times 10^8$ is stable. Furthermore, even though the statistics in this case are not stationary, from the blowup of the time sample and the frequency spectrum we see that two fundamental frequencies are present. These frequencies correspond to transient instabilities of the internal waves near the departing corners and the vertical wall boundary layers. Again, we note the faster attenuation rate of the higher frequency.

A time sample and power spectrum for $Ra = 2 \times 10^8$ are shown in figure 12(*b*). From the figures we see that the flow is strictly periodic with a fundamental frequency $f_i = 630.3$ originating from unstable internal waves. Additionally we observe three higher harmonics within the five orders of magnitude shown.

At $Ra = 3 \times 10^8$ we see from figure 12(*c*) that the flow is quasi-periodic with the two fundamental frequencies $f_i = 737.7$ and $f_w = 8856$, plus harmonics obtained from their linear combinations. The many linear combinations of the fundamental frequencies indicate the strongly nonlinear character of the process. The fundamental frequencies arise from instabilities of the internal waves and the wall boundary layers, respectively. Note that, as mentioned previously, we could not determine unambiguously the value of the larger fundamental frequency by looking at this figure alone. Since the source of these oscillations is located in the vertical wall boundary layers, we examined the spectrum in that region of the flow to determine its value.

As the Rayleigh number is increased to $Ra = 4 \times 10^8$, the flow becomes non-periodic and the spectrum is marked by broadband components, particularly at the lower frequencies. The flow can no longer be described by a small number of well-defined characteristic frequencies; the flow is described as chaotic or weakly turbulent. However, it should be noted that most of the spectral energy still resides in the sharp peaks representing the fundamental frequencies $f_i = 850.2$ and $f_w = 10770$ and their linear combinations, and the flow is still highly ordered, as can be seen in figures 12(*d*) and 3(*d*). Nevertheless, it is important to emphasize the essential qualitative change in the behaviour of the system when the broad components appear in the spectrum. When only discrete frequencies are present, the behaviour of the system is in principle known for all times, but when even a small amount of randomness appears, as evidenced by the broad spectral components, we can no longer hope to make accurate predictions of future values of dependent variables based on the solution at earlier times.

As the Rayleigh number is increased further, the amplitudes of f_i and f_w decrease while the background spectral continuum increases. This can be seen from the power spectrum for $Ra = 10^{10}$ shown in figure 12(*e*). Since the spectrum is continuous it appears that the flow is fully turbulent at this Rayleigh number with most of the energy residing at the lower frequencies. We note that no single frequency stands out. However, the frequencies related to f_i and f_w are still visible at some locations within the cavity. We further note that even though the flow appears to be fully turbulent, the mean flow is symmetric and well behaved. More extensive results in this fully turbulent case will be reported by Paolucci (1989).

The transition from periodic to chaotic flow can be clearly visualized in figure 13, where $T-1$, at the same location as the spectra shown in figure 12, is plotted versus the velocity component u for $Ra = 2 \times 10^8$, 3×10^8, 4×10^8, and 10^{10}.

As can be seen from figures 3(*d*) and 12(*d*), the flow is highly asymmetric as expected when the flow is chaotic. However, similar to figure 5(*d*), we expected that the flow field in figure 3(*c*) would also be asymmetric due to the presence of two fundamental frequencies as shown in figure 12(*c*), and consistent with the results at

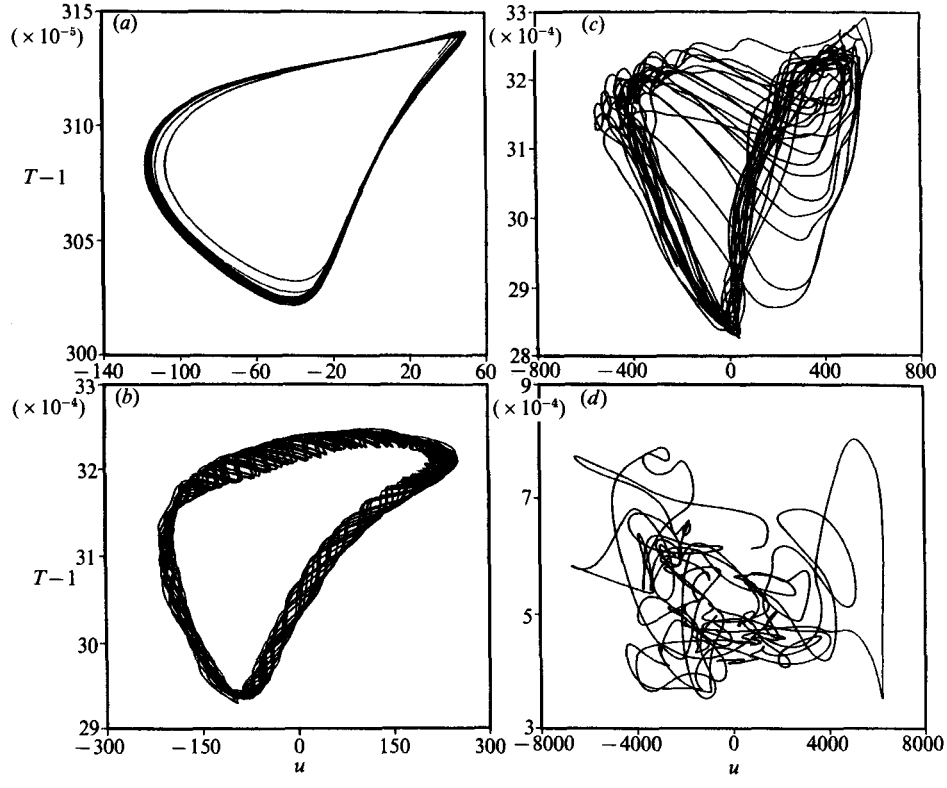

FIGURE 13. Phase space trajectory of temperature versus velocity component u for $A = 1$ at the point $x_i = (1.032 \times 10^{-1}, 8.036 \times 10^{-1})$: (*a*) $Ra = 2.0 \times 10^8$; (*b*) $Ra = 3.0 \times 10^8$; (*c*) $Ra = 4.0 \times 10^8$; (*d*) $Ra = 10^{10}$.

other aspect ratios. However, at this Rayleigh number $f_w/f_i = 12.005$ and additionally f_w/nf_i is an integer for $n \leqslant 4$ indicating that the dominant frequencies are locked, providing a possible explanation for the symmetry in the flow field. The explanation for the slight asymmetry in figure 3(*b*) is not as clear since the spectrum in figure 12(*b*) indicates that only one frequency is present in the flow field at the probed location. However, as noted in table 1, the wall boundary layers were unstable during the transition approaching stationarity, and the presence of this instability is possibly still influencing the slowly changing flow field.

The frequency ratio f_w/f_i varies with increasing Rayleigh number for all computed aspect ratios. Therefore f_w/f_i is in general irrational and the regime with the two modes f_i and f_w is quasi-periodic. As indicated by figure 14(*a–d*), in general the ratios increase sharply near Ra_1 and then vary more gradually with Ra. We remark that because of the lack of resolution with Ra, it is not possible to investigate the extent, if any, of frequency locking. The jump in frequency ratios occurring just below the critical Rayleigh numbers is due to a frequency drop in f_i as can be seen in figure 15(*a–d*). In figure 15(*b*) we also include data from Haldenwang (1986). As can be seen, except for the drop in frequency, our results are in excellent agreement with his. At $Ra = 10^8$, our respective flows approach the same steady state with differing fundamental frequencies which depend on the amplitude of the initial perturbation. The discrepancy in frequency can be explained by the fact that the initial condition he used for his calculation was obtained from a much lower Rayleigh number than

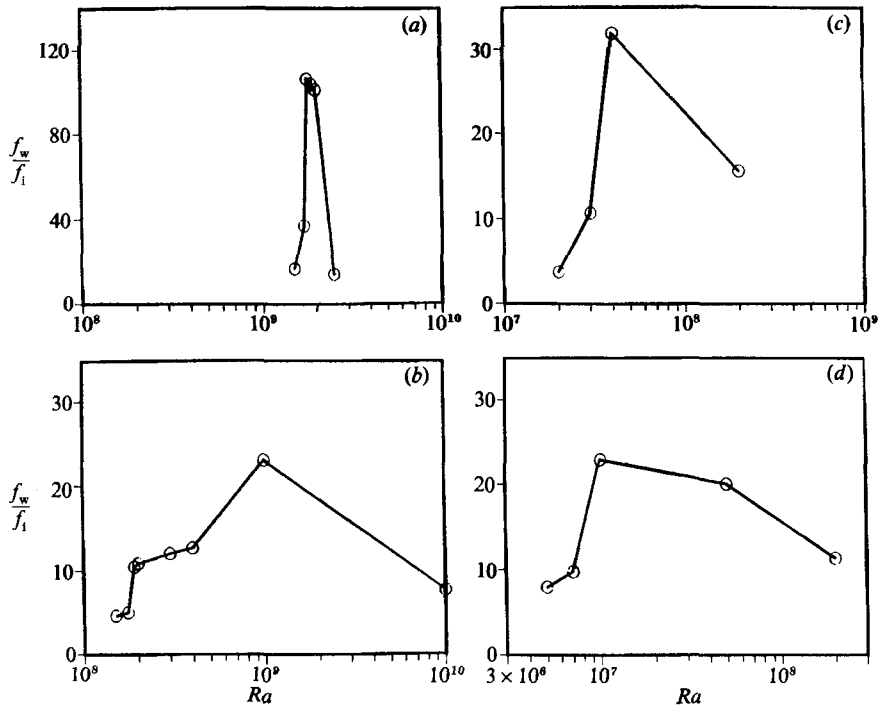

FIGURE 14. Frequency ratio versus Rayleigh number: (*a*) $A = \frac{1}{2}$; (*b*) $A = 1$; (*c*) $A = 2$; (*d*) $A = 3$.

ours. We verified this sensitivity to initial conditions in the vicinity of the critical point by using a lower Rayleigh number result for our initial condition. Note that even though similar qualitative behaviour is exhibited at the different aspect ratios, the amount of frequency drop and the rate of recovery with Rayleigh number does depend on A.

As pointed out previously, the fundamental frequency f_i is due to periodic oscillations of the internal jump. By looking at the time evolution of the flow fields, it appears that the initial drop in f_i near Ra_i occurs when this amplitude becomes large. Large initial perturbations can cause this extreme motion to occur during the transient even for $Ra < Ra_i$, and once the frequency is reduced, it remains locked at the reduced frequency if Ra is sufficiently close to Ra_i. This motion eventually becomes so severe with increasing Ra that due to strong interactions of the jump with the vertical walls the recirculating regions grow and collapse while shedding mass and vorticity. It is the time necessary to rebuild the recirculating regions that is responsible for the frequency drop. The magnitude of the recirculating region before collapse is largest when f_i reaches the lowest values near Ra_i. As Ra is increased further, the shedding of mass occurs more often causing the size of the regions to become smaller, thus f_i increases again with Ra. Finally, when the flow becomes fully chaotic, there are no coherent wave structures remaining in the departing corners and it becomes difficult to identify a frequency with the motion there. The above qualitative physical description of the internal jump near the transition region is similar for the different aspect ratios.

Thorpe (1968) and Keunecke (1970) using linear analyses, examined two-dimensional internal waves in a rectangular container. For a linear density stratification they obtained to first order an expression for the frequency which

depends on the controlling parameters. This expression recast in our nomenclature is given by

$$\hat{f}_i = \frac{C_i}{2\pi}\left\{\frac{Pr\,Ra}{[A(1+(n/p)^2A^{-2})]}\right\}^{\frac{1}{2}}, \tag{3.11}$$

where C_i^2 is directly proportional to the stratification gradient, and p and n are wavenumbers in the horizontal and vertical directions, respectively. Using purely physical arguments, Fischer *et al.* (1979) obtained the identical expression. (Note that Patterson & Imberger (1980), also using physical arguments, obtained (3.11) without the n/p dependence, i.e. $n/p = 1$; furthermore, the A^{-2} dependence in the denominator appears as A^2 in their equation possibly due to a typographic error.) In general, C_i and n/p depend on Pr, Ra, and A.

Additionally, Thorpe (1968) and Keunecke (1970) used liquid filled cavities of known linear density stratification to verify (3.11) experimentally. By varying the frequency of plungers located on the two opposite vertical walls, Thorpe was able to excite waves of small amplitude having different modes. Using the observed values of n and p in (3.11), he found the predicted frequency to be in good agreement with that of the plungers. Furthermore, he studied the nonlinear effects of instability and resulting mixing on the natural frequency of the internal waves. He found that through the different stages of transition the natural frequency of the wave motion was reduced by a non-negligible amount as their amplitudes were increased. He attributed this anomaly to wave-breaking and subsequent mixing. This result is consistent with a decrease in frequency indicated by a third-order correction to (3.11) which he derived. Keunecke, using a more accurate experimental procedure also verified the validity of (3.11).

In our problem, even though the large wave structures in the departing corners are analogous to Thorpe's pistons, we have no direct control of the wave mechanism. Furthermore, because our problem is much more complicated, we are not able to directly observe the different modes that are excited. However, for $A = O(1)$ and $Ra < Ra_i$ the characteristic horizontal and vertical lengthscales of the flow are such that $n/p = 1$, so that by using the measured frequencies we obtain the approximate result that $C_i^2 = 0.91$, consistent with the observed stratifications. For $Pr = 0.71$ we find that C_i is approximately constant and slightly smaller than unity in all cases considered in this paper. Figure 15 shows that (3.11) is in excellent agreement with the data where $n/p = 1$ is expected. In the vicinity of Ra_i, the drop in frequency is evident as the flow approaches steady state, since it becomes unstable during the transient owing to finite initial perturbations. Our results indicate that as Ra_i is approached from below with infinitesimal perturbations, the drop in frequency should occur at Ra_i. The initial decrease in frequency appears to coincide with vortex shedding occurring in the departing corners, consistent with Thorpe's observations.

If we assume that (3.11) remains valid in the transition region with $C_i^2 = 0.91$, then the equation can be used to estimate n/p provided values of f_i from table 1 are substituted for $\hat{f}_i$. The resulting estimates are shown in figure 16(*a–d*) for the different aspect ratios. We note that in all cases we have a sharp increase in n/p near the transition followed by a drop after a maximum is achieved. As can be seen from figures 15 and 16, the sharp increase in n/p corresponds directly to a drop in frequency, while the following decrease in n/p indicates a recovery from the initial frequency drop. The behaviour of n/p may be altered since (3.11) does not contain higher-order effects which may be important during the transition region where wave-breaking and mixing occur.

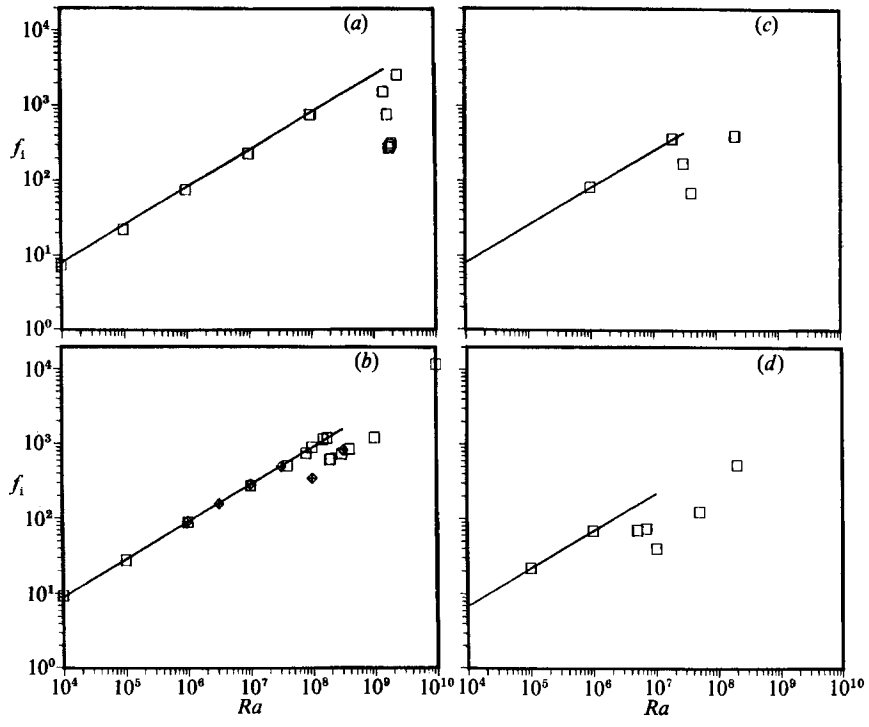

FIGURE 15. Computed internal wave frequencies versus Rayleigh number: (*a*) $A = \frac{1}{2}$; (*b*) $A = 1$; (*c*) $A = 2$; (*d*) $A = 3$. The line is given by (3.11) with $n/p = 1$, and the diamonds in (*b*) are numerical resuts of Haldenwang (1986).

In a similar fashion, much can be learned about the behaviour of the wall instability by examining its frequency response more closely. Again, looking at the related results of Gill & Davey (1969) and Bergholtz (1978) for the buoyancy layer, we arrive at an equation for the critical frequency of the linearly unstable wall boundary layers:

$$\hat{f}_w = C_w \frac{\hat{\alpha}\hat{c}}{8\pi}(4\hat{R}\,Pr\,Ra^2)^{\frac{1}{3}}. \tag{3.12}$$

Values of $\hat{\alpha}$, $\hat{c}$, and $\hat{R}$ were given by Gill & Davey and are repeated in table 2 for convenience. The constant C_w appears to be related to the approximately linear stable stratification. It was introduced here to account for the differences between the idealized conditions in the buoyant layer and our problem. A value of $C_w = 0.91$ is obtained when (3.12) is fitted to our numerical results. Figure 17 displays a comparison of the frequency of wall waves presented in table 1 with those obtained from (3.12). The open circles in the figure are from computations that ultimately lead to steady state (given in parentheses in table 1) while the filled ones result from unsteady solutions. Results of Le Quere & Alziary de Roquefort (1986) for $A = 2$–6 and Haldenwang (1986) for $A = 1$ are included in the figure and represented by squares and diamonds, respectively. It appears that the lowest-frequency results of Le Quere & Alziary de Roquefort start to depart from (3.12) since the hot and cold wall boundary layers can no longer be considered independent for $A \geqslant 6$. As evident from the figure and from the data in table 1, (3.12) is valid well past the critical point. The explanation for this is that as *Ra* is increased, the transition point on the boundary layer moves closer to the entry corner. Thus as long as the flow entering

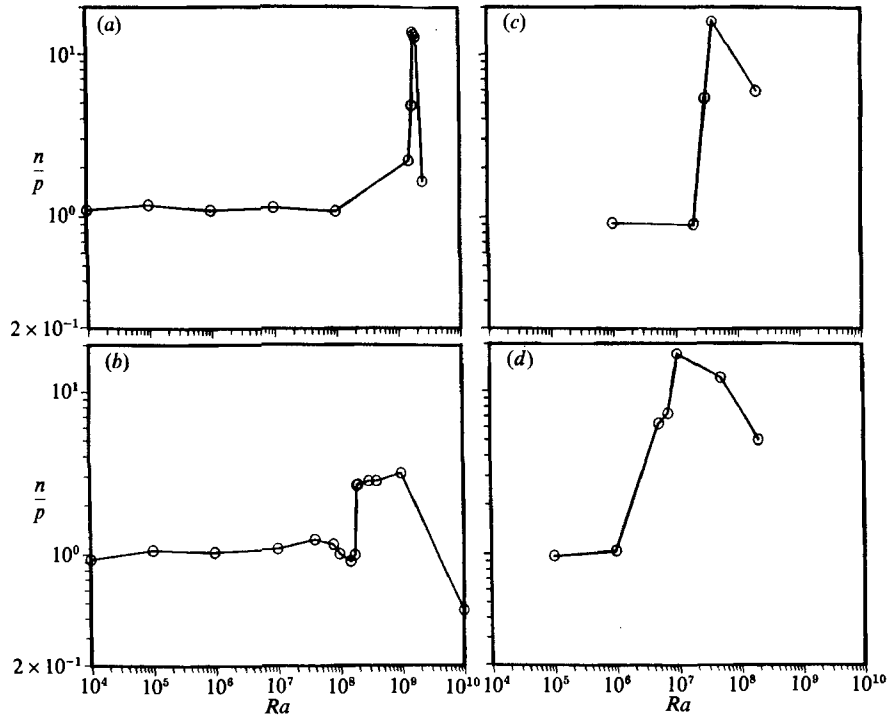

FIGURE 16. Characteristic wavenumber ratio versus Rayleigh number: (*a*) $A = \frac{1}{2}$; (*b*) $A = 1$; (*c*) $A = 2$; (*d*) $A = 3$.

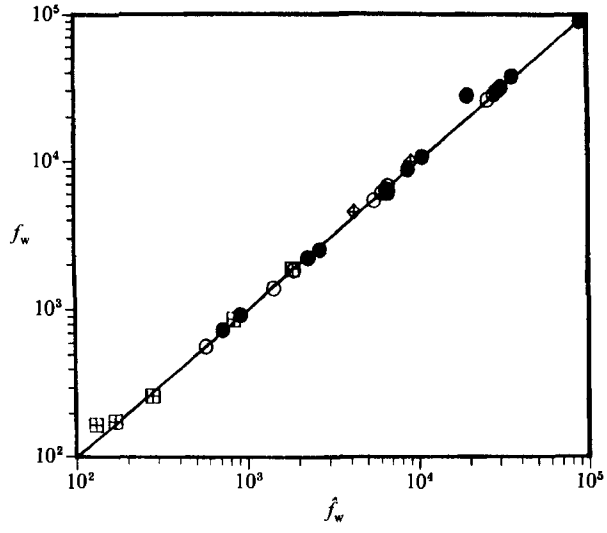

FIGURE 17. Computed wall frequencies *vs.* (3.12): ○, damped when flow became stationary; ●, did not damp when flow became stationary; ⊞, Le Quere & Alziary de Roquefort (1986); ⊕, Haldenwang (1986).

the vertical wall is 'well behaved', a developing laminar boundary-layer region exists and becomes unstable as the local Rayleigh number increases. Therefore, it appears that as long as the transition region is far enough away from the entry and exit corners, this region determines the fundamental frequency of the oscillations. For a fixed aspect ratio, this condition exists for a wide range of $Ra > Ra_w$. Ultimately, as

Ra is increased further, the critical point moves close enough to the entry corner to be affected by it. For $A = 1$ this occurs at Ra near 10^9, since we observe from figure 17 that its computed frequency is significantly above the line given by (3.12).

4. Conclusions

In summary, we have demonstrated by numerical simulation that a variety of dynamic behaviours can occur in two-dimensional convection. With increasing Rayleigh number, the steady convection flow becomes unstable with respect to time-dependent disturbances. In general, for $A \leqslant \frac{1}{2}$ and $A \geqslant 3$ the first time-dependent instability is due to the boundary layers along the vertical walls. However, for $\frac{1}{2} < A < 3$ we first find periodic motion due to internal waves near the departing corners, then quasi-periodic motion (arising from wall boundary layers), aperiodic motion with complex regularity, and finally turbulent motion. The physical mechanisms responsible for the dynamic behaviours are reasonably well understood. We believe that the exposition of the complex dynamic behaviour presented here is possibly important in understanding other flows in natural convection.

One principal finding of this work is that periodic flow is followed by only one additional distinct dynamical regime (quasi-periodic flow with two incommensurate frequencies) prior to the appearance of a chaotic regime. This result is consistent with the predictions of Newhouse, Ruelle & Takens (1978). In addition, even though we restricted the simulations to two spatial dimensions, our results compare favourably with the recent experimental results of Ivey (1984), and analytical/experimental studies of Thorpe (1968), and Keunecke (1970).

Included in our presentation is a discussion of power spectra. The amount of data for the temporal variation of the flow that we have generated is in some cases marginal, but in most cases long periods are covered and Fourier transforms are sufficiently accurate to examine in detail the transitions leading to turbulence. The resulting accuracy is demonstrated by the excellent agreement with the results of Le Quere & Alziary de Roquefort (1986) and Haldenwang (1986). In addition, the numerical results clearly show the importance of the spatial structure of the flow in order to explain the time evolution of this dynamical system.

The results clearly show that for $Pr = 0.71$ and $\frac{1}{2} < A < 3$ internal waves near the departing corners are indeed the source of low-frequency oscillations as suggested by Ivey (1984), and not caused by a 'pile up' of the horizontal intrusions at the far ends as argued by Patterson & Imberger (1980). While the high-frequency oscillations are rapidly attenuated, the low-frequency ones are not, so that their presence is felt throughout the cavity. The low-frequency attenuation, however, is not in general as rapid as suggested by Ivey's experiment with water since in our case their presence is felt throughout the cavity.

We remark that for $A = O(1)$ and small Prandtl numbers, it becomes experimentally difficult to maintain adiabatic boundary conditions on the horizontal walls as Ra becomes large. Furthermore, in a physical experiment, often the Rayleigh number is increased by increasing the temperature difference across the cavity. It has been shown that both of these effects greatly modify the stability of the flow (Le Quere & Alziary de Roquefort 1986; Chenoweth & Paolucci 1986).

Finally we note that one of the main difficulties in the numerical simulations of convection at large Rayleigh numbers is that velocities are large and the problem becomes stiff owing to the $Ra^{-\frac{1}{4}}$ decrease in the boundary-layer thickness. This imposes a severe constraint on the timestep and grid size making calculations

extremely expensive in computer time. Furthermore, because of the presence of internal waves, the transients are very long and the fundamental frequencies are in some cases separated by more than an order of magnitude, necessitating long computations, but with time resolution dictated by the highest frequencies.

This work was performed under the auspices of the US Department of Energy by Sandia National Laboratories, Livermore, California, under Contract No. DE-AC04-76DP00789.

REFERENCES

BERGHOLZ, R. F. 1978 Instability of steady natural convection in a vertical fluid layer. *J. Fluid Mech.* **84**, 743–768.

CHENOWETH, D. R. & PAOLUCCI, S. 1981 On optimizing nonuniform finite-difference grids for boundary regions in transient transport problems. *Sandia National Laboratories Rep.* SAND81-8204.

CHENOWETH, D. R. & PAOLUCCI, S. 1986 Natural convection in an enclosed vertical air layer with large horizontal temperature differences. *J. Fluid Mech.* **169**, 173–210.

ECKERT, E. R. G. & CARLSON, W. O. 1961 Natural convection in an air layer enclosed between two vertical plates with different temperatures. *Intl J. Heat Mass Transfer* **2**, 106–120.

ELDER, J. W. 1965 Turbulent free convection in a vertical slot. *J. Fluid Mech.* **23**, 99–111.

FENSTERMACHER, P. R., SWINNEY, H. L. & GOLLUB, J. P. 1979 Dyamical instabilities and the transition to chaotic Taylor vortex flow. *J. Fluid Mech.* **94**, 103–128.

FISCHER, H. B., LIST, E. J., KOH, R. C. Y., IMBERGER, J. & BROOKS, N. H. 1979 *Mixing in Inland and Coastal Waters.* Academic.

GILL, A. E. & DAVEY, A. 1969 Instabilities of a buoyancy-driven system. *J. Fluid Mech.* **35**, 775–798.

GOLLUB, J. P. & BENSON, S. V. 1980 Many routes to turbulent convection. *J. Fluid Mech.* **100**, 449–470.

GORMAN, M. & SWINNEY, H. L. 1982 Spatial and temporal characteristics of modulated waves in the circular Couette system. *J. Fluid Mech.* **117**, 123–142.

GRÖTZBACH, G. 1982 Direct numerical simulation of laminar and turbulent Bénard convection. *J. Fluid Mech.* **119**, 27–53.

HALDENWANG, P. 1986 Unsteady numerical simulation by Chebyshev spectral methods of natural convection at high Rayleigh numbers. *Proc. ASME Winter Annual Meeting, ASME HTD*, vol. 60, pp. 45–51. Anaheim, California.

IVEY, G. N. 1984 Experiments on transient natural convection in a cavity. *J. Fluid Mech.* **144**, 389–401.

IYER, P. A. 1973 Instabilities in buoyancy-driven boundary-layer flows in a stably stratified medium. *Boundary-Layer Met.* **5**, 53–66.

KÁLNAY DE RIVAS, E. 1972 On the use of nonuniform grids in finite-difference equations. *J. Comp. Phys.* **10**, 202–210.

KEUNECKE, K.-H. VON 1970 Stehende interne wellen in rechteckigen becken (Standing internal waves in rectangular tanks). *Deutsche Hydrographische Zeitschrift* **23**, 61–79.

LE QUERE, P. & ALZIARY DE ROQUEFORT, T. 1985*a* Computation of natural convection in two-dimensional cavities with Chebyshev polynomials. *J. Comp. Phys.* **57**, 210–228.

LE QUERE, P. & ALZIARY DE ROQUEFORT, T. 1985*b* Transition to unsteady natural convection of air in differentially heated vertical cavities. In *Numerical Methods in Laminar and Turbulent Flow*, pp. 841–852. Swansea: Pineridge.

LE QUERE, P. & ALZIARY DE ROQUEFORT, T. 1986 Transition to unsteady natural convection of air in differentially heated vertical cavities. *Proc. ASME Winter Annual Meeting, ASME HTD*, vol. 60, pp. 29–36. Anaheim, California.

LIGHTHILL, J. 1978 *Waves in Fluids.* Cambridge University Press.

LILLY, D. K. 1965 On the computational stability of numerical solutions of time-dependent non-linear geophysical fluid dynamics problems. *Mon. Weather Rev.* **93**, 11–26.

MORDCHELLES-REGNIER, G. & KAPLAN, C. 1963 Visualization of natural convection on a plane wall and in a vertical gap by differential interferometry. Transitional and turbulent regimes. In *Heat Transfer Fluid Mech. Inst.* pp. 94–111. Stanford University Press.

NEWHOUSE, S., RUELLE, D. & TAKENS, P. 1978 Occurrence of strange axiom A attractors near quasi periodic flows on T^m, $m \geqslant 3$. *Commun. Math. Phys.* **64**, 35–40.

OTNES, R. K. & ENOCHSON, L. 1978 *Applied Time Series Analysis*. Wiley.

PAOLUCCI, S. 1989 Direct numerical simulation of turbulent natural convection in an enclosed cavity. *J. Fluid Mech.* (submitted).

PATTERSON, J. & IMBERGER, J. 1980 Unsteady natural convection in a rectangular cavity. *J. Fluid Mech.* **100**, 65–86.

ROBERTS, G. O. 1970 *Computational Meshes for Boundary Layer Problems* (ed. M. Holt). Lecture Notes in Physics, vol. 8, pp. 171–177. Springer.

THORPE, S. A. 1968 On standing internal gravity waves of finite amplitude. *J. Fluid Mech.* **32**, 489–528.

TURNER, J. S. 1973 *Buoyancy Effects in Fluids*. Cambridge University Press.